MEASUREMENTS OF THE OPPOSITION EFFECT IN THE VISIBLE AND NEAR-INFRARED USING AN IMPROVISED IMAGING SPECTROPOLARIMETER

by

Kyle A. Foster
A Thesis
Submitted to the
Graduate Faculty
of
George Mason University
in Partial Fulfillment of
The Requirements for the Degree
of
Master of Science
Earth Systems Science

Committee:

____________________	Dr. Guido Cervone, Thesis Director
____________________	Dr. Ronald G. Resmini, Committee Member
____________________	Dr. Sheryl Luzzadder-Beach, Committee Member
____________________	Dr. Peggy Agouris, Department Chair
____________________	Dr. Timothy L. Born, Associate Dean for Student and Academic Affairs, College of Science
____________________	Dr. Vikas Chandhoke, Dean, College of Science
Date: 11/21/12	Fall Semester 2012 George Mason University Fairfax, VA

Measurements of the Opposition Effect in the Visible and Near-Infrared Using an Improvised Imaging Spectropolarimeter

A thesis submitted in partial fulfillment of the requirements for the degree of Master of Science at George Mason University

by

Kyle A. Foster
Bachelor of Science
Rochester Institute of Technology, 2008

Director: Guido Cervone, Professor
Department of Geography and GeoInformation Science

Fall Semester 2012
George Mason University
Fairfax, VA

DEDICATION

To my wife Courtney and my daughter Claire, for sticking with me through my adventures in grad school. Thank you for all your love, patience, and support; Daddy can come outside and play now.

ACKNOWLEDGEMENTS

This document is the culmination of several years of effort, and one of the most difficult tasks I’ve ever completed. I did not work in a vacuum, however, and there are a number of formidably skilled people who deserve recognition for their contributions.

My journey at George Mason University started one year after the conclusion of my B. S. in Imaging Science at the Rochester Institute of Technology, an adventure in itself. For their support in the latter achievement—which built the groundwork for the former—I am forever grateful to Dr. Jon Arney, Sue Chan, Dr. Carl Salvaggio, Nina Raqueno, Lon Smith, and Dr. Spencer Meredith.

Pursuing a graduate degree while working full time requires coordination with one’s coworkers, and mine were extremely accommodating. Brandon Migdal, Joy Van de Mortel, Dave Jones, Erik Shepard, Dan O’Connor, Dave Wellman, Louis Atchison, Dan Brennan, and a bevy of other teammates have my thanks for their flexibility, understanding, and support.

In approximate temporal order, I thank the following cast of extraordinarily patient people: Mark Bowman, Dr. David Wong, and Dr. Anthony Stefanidis for their extremely valuable guidance, insight, and support during my admission; the faculty and staff of the GGS Department, for the loan of the SOC700 and providing all my classes; Dr. Amin Jazaeri of the Physics Department, for the SOC700 training; Marissa Resmini, Dr. Whitney Nelson, and Dr. Tim Marshall for their support in early field collections; Dr. Herschel Burstyn, for early data analysis support; Jacek Radzikowski, for the loan of the lab tripod; Dr. David Allen, for loaning the PTFE slab and calibrated Spectralon disk, as well as for his positive review of my setup; Dr. Mary Kappus, for her donation of a material sample, her ever-sage advice, and her general friendship; Dr. Devin White and May Casterline, for helping me troubleshoot the ENVI batch scripts vital to my processing; Dr. David Chenault and Leif Hendricks, for taking time at SPIE Defense 2012 to help a harried grad student the day before his defense; Laura Lynn and Bridget Baker, for helping to edit this juggernaut; Teri Fede, for her administrative support; and all the rest of my friends and family—especially Mike & Julie Denning, fellow RIT alumni—for their moral support and shoulders to lean upon.

Several companies and organizations were also critical in this effort. Sabre Systems and the United States Geospatial Intelligence Foundation (USGIF) were generous in their funding of awards I received through the GGS Department; the former organization supported my award as a runner-up for “Best Graduate Poster with Presentation” in the November 2011 GIS Day Poster Competition, while the latter funded the award for “Outstanding MS Graduate Student, 2012.” Bluemont Vineyard of Bluemont, VA literally empowered some of my 2009 measurements. Midwest Supplies, Beers of the World in Rochester, NY, and Jay’s Brewing in Clifton, VA all helped me with materials for my parallel experiments in homebrewing. Dogfish Head Alehouse in Chantilly, VA was always there with “grad school fuel” when my own wasn’t ready yet; if “off-centered ales for off-centered people” isn’t an apt description of grad school, I don’t know what is.

My thesis would be nothing without my committee, to whom I owe so much. My advisor, Dr. Guido Cervone, was tireless in helping to consider new twists and approaches to various issues, and in sharing “new daddy” stories and tactics. The globe-trotting Dr. Sheryl Luzzadder-Beach was always ready with words of enthusiasm, shared keen insight on how to navigate university processes, and was vital in arranging lab space. Dr. Ron Resmini was a critical catalyst in this work from the start, from the first measurements in 2009 through to its conclusion, taking on a hefty share of conceptualization, review, editing, and the sort of irreplaceable “reality check” mentoring needed by all grad students—or at least one, anyway. Thank you all.

Courtney Foster and Claire Foster—my wife and daughter, respectively—had hands in much of the above, and more. (Two of those hands may have been covered in peanut butter and pine sap.) A dedication isn’t enough; always and forever, my love and thanks.

-KF, 9/10/12

TABLE OF CONTENTS

LIST OF TABLES

LIST OF FIGURES

Figure Page

LIST OF EQUATIONS

LIST OF ABBREVIATIONS AND SYMBOLS

Acousto-optical tunable filter .... AOTF
Advanced Earth Observing Satellite .... ADEOS
Advanced Visible/Infrared Imaging Spectrometer .... AVIRIS
Angle .... θ
Blue .... B
Centimeter .... cm
Circular polarization .... CP
Degree of linear polarization .... DOLP
Electromagnetic .... EM
George Mason University .... GMU
Green .... G
Ground sample distance .... GSD
Hyperspectral imaging/imagery .... HSI
Land use/land cover .... LULC
Landsat 7 Enhanced Thematic Mapper Plus .... ETM+
Linear polarization .... LP
Liquid crystal tunable filter .... LCTF
Long-wave infrared .... LWIR
Measurement[s] .... meas
Mid-wave infrared .... MWIR
Milliwatt .... mW
Multispectral imaging/imagery .... MSI
Nanometer .... nm
National Institute of Standards and Technology .... NIST
Near-infrared .... NIR
Phase Angle .... φ
Photoelastic modulator .... PEM
Polarimetric imaging/imagery .... PI
Polytetrafluoroethylene .... PTFE
Principal components analysis .... PCA
Quartz tungsten halogen .... QTH
Red .... R
Reference .... ref
Second .... s
Short-wave infrared .... SWIR
Signal-to-noise ratio .... SNR

Spectropolarimetric imaging/imagery .... SPI
Steradian .... sr
Surface Optics Corporation........ SOC
Temperature .... temp
Temperatures........ temps
Thematic Mapper .... TM
Ultra-high performance concrete .... UHPC
Ultraviolet .... UV
Visible and near-infrared .... VNIR
Watt........ W
With........ w/
Without .... w/o
Wavelength .... λ

ABSTRACT

MEASUREMENTS OF THE OPPOSITION EFFECT IN THE VISIBLE AND NEAR-INFRARED USING AN IMPROVISED IMAGING SPECTROPOLARIMETER

Kyle A. Foster, MS

George Mason University, 2012

Thesis Director: Dr. Guido Cervone

Spectropolarimetry is a remote sensing technique that combines both spectral and polarimetric measurements. It is already well-established in the astronomical community as an indispensable tool, permitting characterization of dust clouds and stars, and enhancing observations of planetary bodies. One such noteworthy phenomenon is the opposition effect, wherein a planetary body such as the Moon exhibits a surge in reflected intensity as the phase angle—an angle between the Sun, the Moon, and the observer—decreases to below approximately five degrees. Astronomical and laboratory investigations into the opposition effect reveal that the light of this surge often has a polarized component.

The terrestrial remote sensing community is starting to develop an interest in spectropolarimetry. Spectral and polarimetric measurements alone, while useful in their diverse applications, stand to benefit from the added dimensionality that

spectropolarimetric measurements provide. Examples of applications that benefit from spectropolarimetric measurement include environmental monitoring, search & rescue, and countering denial and deception techniques. To that end, an improvised imaging spectropolarimeter sensitive in the visible and near-infrared spectrum has been developed by attaching a linear polarization filter to a SOC700 hyperspectral imaging system for use in further development of spectropolarimetric applications.

The results of three research objectives are reported upon. First, validation of the operation of the improvised imaging spectropolarimeter and the resulting data calibration and processing techniques, including generating Stokes parameter imagery, is successfully completed. Second, demonstrating that the improvised system is capable of observing the opposition effect in a laboratory setting is also confirmed. Third, the improvised system is used to characterize various materials—including rare earth element oxides and ultra-high performance concrete—in various phase angle geometries, with the intent of determining whether the polarized component of the opposition effect yields sufficient additional information for material detection and identification.

CHAPTER ONE – INTRODUCTION AND BACKGROUND

In simple terms, remote sensing is the non-contact observation of the transaction of information between two points separated by a distance. The currency is energy in its many forms: potential, kinetic, thermal, electrical, and more. For observations of the Earth and its neighbors in space, the most commonly used medium for study is light, or in a more general sense, electromagnetic (EM) radiation. Electromagnetic radiation is absorbed by and emitted from, transmitted by, or reflected/scattered by a given object of interest, with some of the emitted or reflected energy eventually captured by a sensor. This captured energy is converted into information by the sensor and presented to a user for interpretation.

Electromagnetic radiation is created by the activity of charged particles moving and interacting with each other. It is so named because it is comprised of electric and magnetic field components that oscillate orthogonally to one another at a right angle to the direction of how they propagate through space (Hecht, 1998). A diagram of an electromagnetic wave is shown in Figure 1.

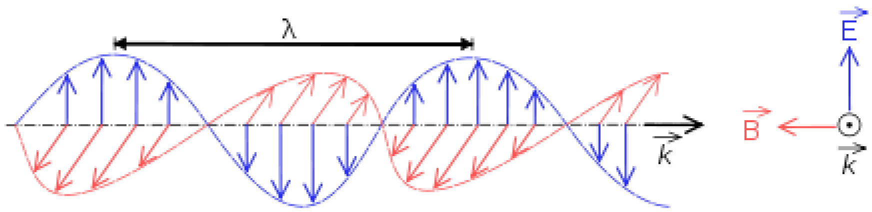

Figure 1 A representation of electromagnetic radiation propagating through space (Boutet, 2007)

In Figure 1, $\vec{k}$ is a vector for the direction of propagation for the electromagnetic wave. $\vec{B}$ and $\vec{E}$ are vectors for the magnetic and electric field components of the wave, respectively. The Greek letter λ denotes wavelength, which is described later in this chapter. Figure 1 shows the electric and magnetic field components are orthogonal and in phase.

Depending upon the application, electromagnetic radiation can be considered to behave either as a particle—often referred to as a photon—or as a wave. For the purposes of this thesis, the wave aspect of this dual-natured phenomenon is most often considered.

Properties of Electromagnetic Waves, and their Measurement

All waves, including electromagnetic waves, have certain measureable properties. Properties of waves include amplitude, phase, frequency, wavelength, polarization, and speed. Measurement of EM waves to obtain information about an object or target depend on the discrimination of energy from the object on the basis of these properties. The properties of particular relevance to this thesis are wavelength and polarization.

Wavelength

Wavelength as a discriminating factor for the measurement of electromagnetic radiation is very well established, demonstrable in the vast numbers of sophisticated imaging systems currently in use around the world and throughout the Solar System (Shaw & Burke, 2003) (McEwen et al., 2007) (Blackburn, Buratti, & Ulrich, 2011).

Wavelength is a measure of distance, specifically the span between adjacent cycles of identical corresponding parts of the wave's phase. This is often simplified in description as distance from peak to peak of the electric field vector of an electromagnetic wave. An example is presented in preceding pages in Figure 1, denoted by the Greek letter λ.

The continuum of wavelengths for electromagnetic radiation yields a concept called the electromagnetic spectrum. Different parts of this spectrum interact with the surrounding environment in unique ways, and are loosely organized into different groups or regimes. Figure 2 provides an annotated graphical representation of the electromagnetic spectrum.

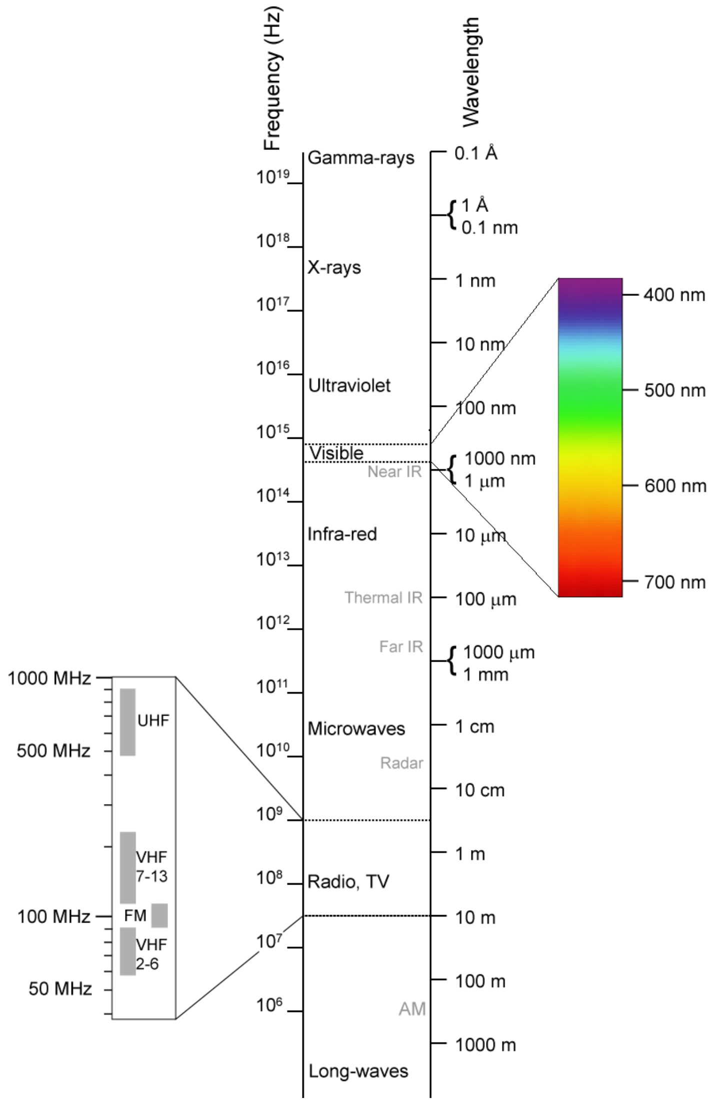

Figure 2 The electromagnetic spectrum (Penubag, 2008)

Polarization

Polarization, though studied for centuries (Tyo et al., 2006), has until relatively recently been far less commonly used as a discriminating factor, particularly for terrestrial remote sensing applications. Instead, polarization has often been treated as something to be neglected or rendered inconsequential as much as possible, to avoid any potential interference polarization factors might have in the design of sensors and the interpretation of data from those sensors (Schott, 2009).

Polarization describes the orientation of an electromagnetic wave about its transmission axis as it propagates through space. The description depends on the behavior of the orthogonal vector components of the electric field vector of the electromagnetic wave, which describe waves of their own as they propagate. There are two special descriptive cases and one general descriptive case for polarization, the latter of which is more easily grasped after considering the former. When the electric field components are in phase, their vector sum oscillates from one extent to its opposite and transcribes a line as the wave propagates. This special condition is called linear polarization. When the electric field components are out of phase by $\pi/2$, a condition referred to as being "in quadrature," the vector sum of the fields transcribes a circle as the wave propagates. This special condition is called circular polarization. When the electric field components are not in phase or quadrature but at some arbitrary phase relationship to one another, the vector sum transcribes an ellipse with parameters derived from the phase difference and amplitudes of the electric field components. This general case is called elliptical polarization (Schott, 2009). Figure 3 provides depictions of how the electric field components create vector sums that demonstrate linear, circular, and elliptical polarization.

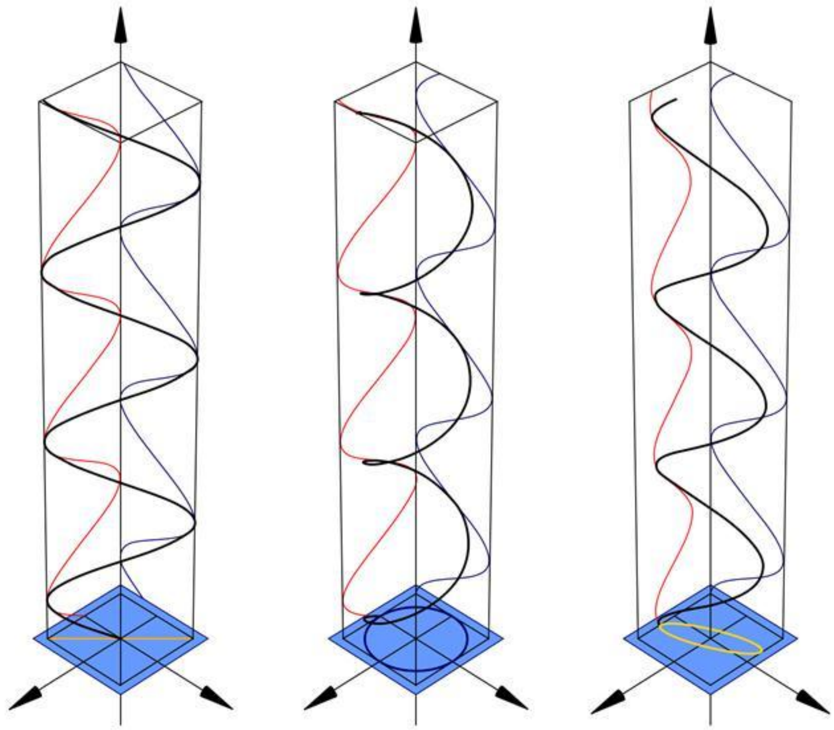

Figure 3 From left to right: linear polarization, circular polarization, and elliptical polarization (Inductiveload, 2007)

Many depictions of polarization show a single wave of electromagnetic radiation of a single polarization type incident upon an object at a time. However, most natural and artificial sources of electromagnetic radiation produce large quantities of such waves, with a great diversity of polarization states, geometries, and positions, including superposition of different waves. Two different terms are employed to describe this single phenomenon: unpolarized light, and randomly polarized light. The state of "unpolarization" is used to describe an aggregate of waves that do not demonstrate any particular preference for a given polarization state. Random polarization describes the same exact condition, while emphasizing the fact that this aggregate is in fact some number of waves that exhibit certain polarization states, and that their aggregate does not promote any over the rest (Schott, 2009).

Most natural sources produce randomly polarized light. To introduce a measurable preference toward a specific non-random polarization state, something must interact with the waves of light to change the relative phases of the electric field components. This is caused by the interaction of the light with matter on a variety of scales, ranging from the atomic to the macroscopic. Light can be reflected/scattered, refracted, absorbed (and re-emitted spontaneously), diffracted, or transmitted when interacting with a material in its path. These interactions variably change the relative phase of the electric field components of the wave, and thus alter the polarization state of the light (Hecht, 1998).

To measure and quantify a particular kind of polarization, there must be some means of discriminating polarization states. There are a variety of filtration methods that are employed to this end. Two natural phenomena that can be used for this purpose are birefringence and dichroism. Birefringence occurs when a non-cubic crystalline structure refracts two orthogonal linear polarization components of a single beam of light through different paths in the material. The different paths of the refracted, polarized light produce a “double image” to an observer (Hecht, 1998). Dichroism occurs when a material selectively absorbs or transmits electromagnetic waves of varying polarization states. Calcite is a material popularly used to demonstrate birefringence, while tourmaline is typically provided as an exemplar of dichroism. However, tourmaline's dichroistic properties are also wavelength dependent (Falk, Brill, & Stork, 1986).

Linear polarization filters—sometimes called polarizers or analyzers—are optical components that permit one particular variety of linear polarization to pass while reducing or obscuring others. Some designs employ the inherent properties of birefringence or dichroism in a particular material to achieve this. Another technique is the use of grids of parallel wires, filaments, or lithographic etches and uniformly spaced on the order of the size of the wavelength of electromagnetic radiation to be filtered (Hecht, 1998). Electromagnetic waves that are linearly polarized perpendicular to the filaments of the grid are passed through the filter. The polarization angle of these waves describes what is called the transmissive axis of the filter. Electromagnetic waves that are linearly polarized at angles non-perpendicular to the grid are subdued to an extent proportional to the cosine of the angle between the linear polarization of the wave and that of the transmission axis (Schott, 2009). Figure 4 below provides a simplified visual representation of how such a wire grid filters linearly polarized light.

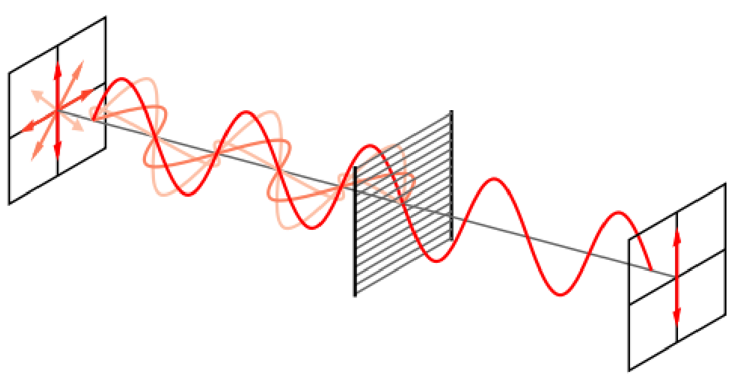

Figure 4 Example of a wire grid linear polarization filter (Mellish, 2006)

Most common circular polarization filters use wire grid linear polarization filters preceded in the light path by a construct known as a quarter wave plate. Typically composed of a highly polished birefringent material of a particular thickness, a quarter wave plate is a material that retards one of the electric field components of an electromagnetic wave by $\pi/2$, or a quarter wave. When circularly polarized light passes through a quarter wave plate, the light becomes linearly polarized. The same is true in reverse, as well: linearly polarized light passing through a quarter wave plate is converted to circularly polarized light (Fowles, 1975). The polarization angle of the linearly polarized light that comes through the quarter wave plate depends upon the chirality of the circularly polarized light incident on the plate, and the angular orientation of the plate; similar to the transmission axis of a wire grid linear polarization filter, a quarter wave plate has a fast axis and a slow axis that determine which electric field component is retarded by $\pi/2$. The linear polarization angle is typically halfway between the angles of the fast and slow axes of the quarter wave plate. However, different input chiralities result in opposite linear polarization angles for output (i.e., 45° vs. 135°). Thus, by adding a linear polarization filter in the optical path after a quarter wave plate, a circular polarization filter is formed, allowing electromagnetic waves that start out as circularly polarized with a certain chirality to be discriminated from waves with other kinds of polarization (Fowles, 1975). Figure 5 shows how a circular polarization filter operates using the above principles.

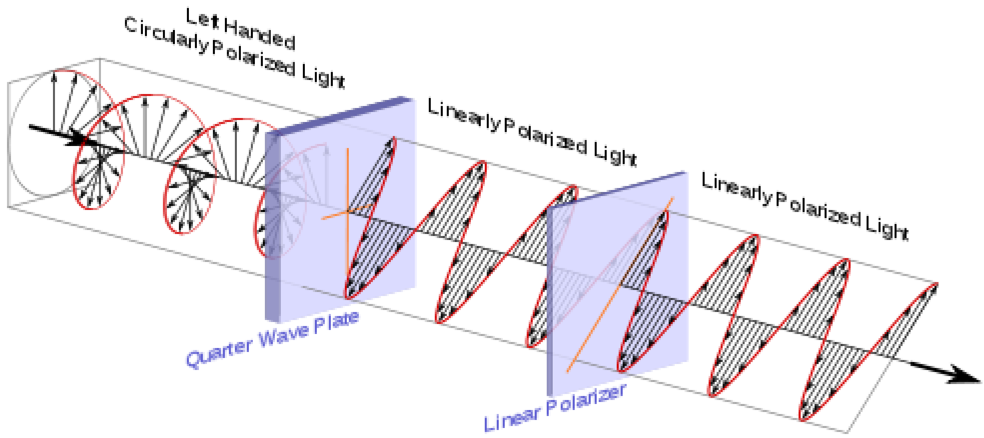

Figure 5 A circular polarization filter, created through a combination of a quarter wave plate and a linear polarization filter (Dave3457, 2010)

The wave component retardation factor of any wave plate is a function of the wavelength of the incident wave; this means that a traditional quarter wave plate is only truly such at a specific wavelength, and that it retards a different percentage of the wave component as a function of the change in wavelength (Webb, 1997). Special designs, such as the Pancharatnam "superchromatic" quarter wave plate, have been developed that filter circularly polarized light over a much larger spectral range than a traditional arrangement (Goodrich, Cohen, & Putney, 1995).

Useful Polarization Concepts

Brewster's Angle

The index of refraction is a property of a material that describes how the velocity of light in the medium relates to the velocity of light in a reference medium, such as in a perfect vacuum. The path of light traveling through a medium of a particular refractive index is altered when incident upon a boundary with a material with a different refractive index. The alteration of the path can be predicted by Snell's Law, which combines the geometry of the incidence of the ray upon the boundary and the indices of refraction for the two media forming a boundary in a simple trigonometric equation. Snell's Law is presented below as Equation 1:

Equation 1 Snell's Law

$$n_1 \sin(\theta_1) = n_2 \sin(\theta_2)$$

where n_1 and n_2 represent the indices of refraction for two media, and θ_1 and θ_2 represent the angles of incidence of the rays on the boundary as measured from the boundary normal.

Refractive indices are generally wavelength-dependent; i.e., the refractive index of a material varies depending upon the wavelength of the light incident upon it. Refractive indices can also be polarization-dependent as well, though this dependence is also related to the geometry of the light wave's incidence upon the boundary of the media. Brewster's Law, presented in Equation 2, provides one means by which the relationship between indices of refraction and the geometry of incidence affects the polarization state of light:

Equation 2 Brewster's Law

$$\theta_B = \arctan\left(\frac{n_2}{n_1}\right)$$

where n_1 and n_2 again represent the indices of refraction for two media at a boundary, while θ_B is a specific measure known as Brewster's angle, again measured from the normal of the boundary. Randomly polarized light incident upon a boundary at Brewster's angle is partially reflected and partially refracted. The light that is refracted through the second medium demonstrates a slight polarization, while the light that is reflected back into the original medium is strongly linearly polarized parallel to the boundary surface. Figure 6 depicts this change in the polarization state of light incident upon a boundary at the material's Brewster angle.

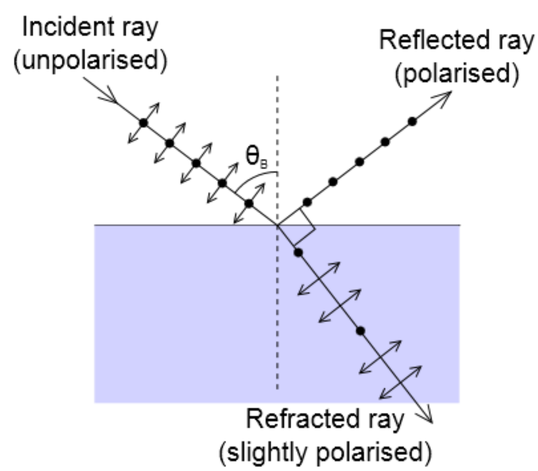

Figure 6 Depiction of light incident upon a boundary at Brewster's angle, and the resulting effect upon polarization (Pajs, 2007)

Polarization Ratio

An extensive literature exists in the field of astronomical remote sensing relating to the polarization of light. One of the most commonly utilized relationships in this literature is the linear polarization ratio equation, presented as Equation 3:

Equation 3 The linear polarization ratio equation

$$P = \frac{I_{\perp} - I_{\parallel}}{I_{\perp} + I_{\parallel}}$$

where P represents the total degree of linear polarization, and $I_{\perp}$ and $I_{\parallel}$ represent the intensity of light measured with linear polarization angles perpendicular and parallel to the scattering plane, respectively (Tishkovets, 1997). The scattering plane is defined as the plane that includes the path of a beam of light upon a target, and the light that scatters directly back to an observer. Figure 7 shows a scattering plane orientation.

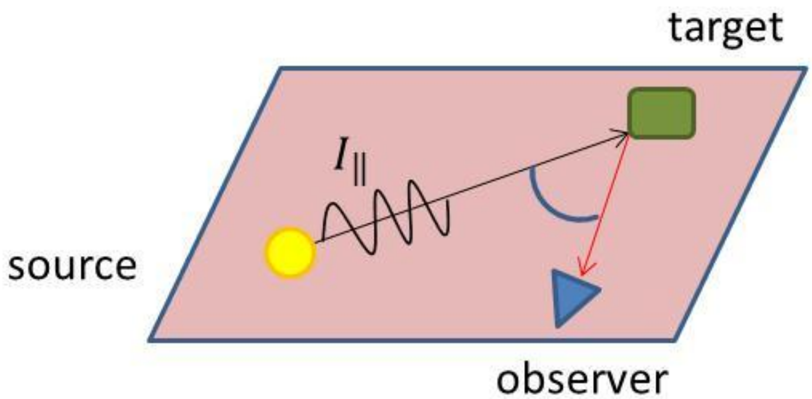

Figure 7 A representation of the scattering plane, which contains the angle between source, target, and observer; $I_{||}$ is in-plane, while $I_{\perp}$ (not shown) is orthogonal to the plane in terms of polarization

In the scattering plane in Figure 7, only the light with linear polarization parallel to the scattering plane ($I_{||}$) is shown. The light with linear polarization perpendicular to the scattering plane ($I_{\perp}$) is not shown, but follows the same path as $I_{||}$, with oscillation orthogonal to that of $I_{||}$, which in this representation would be into and out of the page.

The terms "negative polarization" or "negative polarization ratio" are common in much of the astronomical literature. They refer to the value of P in Equation 3 when $I_{||}$ is the dominant linear polarization intensity for an observation. The placement of $I_{||}$ in the equation forces P to a negative value when $I_{||}$ is greater than $I_{\perp}$ (Tishkovets, 1997).

Umov Effect

The reflection coefficient, or albedo, of an object is a ratio of the intensity of the light reflected by the object to the intensity of the light incident upon the object. Albedo is a wavelength-dependent property. As an object's albedo increases for a specific wavelength, light is increasingly reflected by the object at that wavelength; as albedo decreases for a specific wavelength, less light is reflected (Dobos, 2006).

The Umov effect is a principle of polarization that states a decrease in the albedo of an object yields an increase in the degree of polarization in the light reflected (Schott, 2009). One explanation of the Umov effect in quantities of particulates is that increased inter-particle multiple scattering increases albedo, and decreases the maximum linear polarization, as increased scattering introduces greater diversity of different polarization angles and draws closer to a state of random polarization. Consequently, this explanation brings a large number of factors into play, such as particle size, shape, and density, and suggests that for varying particulates, the Umov effect is not always prominent (Zubko et al., 2011). For solid surfaces, the general concept is that low albedo yields high polarization, though this may be more dependent upon the diffuse scattering component of the surface than the specular component (Eyler, 2009).

Relevant Remote Sensing Techniques

Polarimetric Imaging (PI)

Collecting, discriminating, and interpreting EM waves from a given scene on the basis of their polarization is a technique known as polarimetric imaging, or PI. The technique can be applied throughout many different parts of the EM spectrum for different purposes. In the visible and near-infrared (VNIR), PI can be used for distinguishing manmade and/or metallic materials from vegetative or otherwise natural backgrounds, an appealing consideration for both search and rescue and camouflage detection (Schott, 2009). For this spectral regime, the dominant influence is reflected light. In the thermal infrared part of the EM spectrum, there is a far stronger emissive component; that is, various materials emit polarized electromagnetic radiation as a function of their temperature and surface geometries. In the case of radar, an active remote sensing technique utilizing microwave and radio wavelengths of the EM spectrum, horizontal and vertical linear polarization angles can be transmitted and received to aid in object detection and characterization, scene and environment contrast improvements, and other factors (Tyo et al., 2006).

Polarimetric imaging systems are also employed for observations of the Earth's atmosphere and aerosol detection and characterization. A space-based instrument design called POLDER, or Polarization and Directionality of the Earth's Reflectances, flew on two different Advanced Earth Observing Satellite (ADEOS) missions in the late 1990s and early 2000s (Deschamps et al., 1998). The instruments measure eight spectral bands, with a filter wheel in place to rotate between three different polarizers on three of the VNIR spectral bands, allowing computation of the polarization ratio for terrestrial scenes. During their operational missions, the POLDER instruments were vital in using polarization to develop global tropospheric aerosol maps, distinguishing between water droplets and ice in clouds, and measuring cloud level pressures (Breon et al., 2002).

Multispectral Imaging (MSI) and Hyperspectral Imaging (HSI)

Collecting, discriminating, and interpreting EM waves from a given scene on the basis of their wavelength is a technique known as imaging spectroscopy, or spectral imaging. There are two principal forms of spectral imaging: multispectral imaging (MSI), and hyperspectral imaging (HSI).

Multispectral imaging describes the collection of EM waves in anywhere from three to several dozen broad spectral bands that need not be uniform in spectral bandwidth, spectral proximity, or spatial resolution. Multispectral bands are selected during the sensor design phase to emphasize sensitivity to particular phenomena associated with specific wavelengths. A single multispectral band may cover a broad spectral range and represent it as a single output (Shaw & Burke, 2003).

Hyperspectral imaging describes the collection of EM waves in dozens to hundreds of spectral bands that are uniformly sized and spaced in terms of spectral bandwidth, all with the same spatial resolution. A plot of spectral band outputs from a hyperspectral sensor for a given spatial pixel can be calibrated into a spectral signature resembling one measured with a laboratory spectrometer, while that of a multispectral sensor generates a much lower spectral resolution approximation (Schott, 2007).

Multispectral imaging is used in a broad array of applications. Airborne and spaceborne multispectral systems of medium to coarse spatial resolution (dozens of meters to kilometers per pixel) are often used for land use/land cover (LULC) analyses, weather and climate modeling, vegetative health monitoring, coastal health monitoring, wildfire detection and monitoring, and more. The Thematic Mapper (TM) and Enhanced Thematic Mapper Plus (ETM+) instruments onboard Landsats 5 and 7, respectively, are examples of medium resolution spaceborne multispectral systems, collecting spectral information in 7 and 8 spectral bands, respectively. Pixels within these bands have ground sample distances (GSDs) ranging from 15 meters to 120 meters, depending upon the instrument and band in question, as well as the altitude of the satellites (approximately 700 kilometers) (NASA, 2012).

Hyperspectral imaging is also used in a diverse set of applications. Airborne and spaceborne HSI systems are used to identify chemical signatures in rocks and soil, aerosol plumes, and water surfaces. Like MSI, HSI can also be used for vegetative mapping and health monitoring, coastal health monitoring, and other similar environmental applications. The ability to generate spectra for any part of a scene allows for the possibility of discriminating and identifying materials at potentially very long distances (Shaw & Burke, 2003). A robust literature continues to grow for the use of a wide variety of ground, aerial, and space-based HSI systems for determining the chemical composition of various solids, liquids, and aerosols. A popular example of a hyperspectral imaging system is AVIRIS, the Airborne Visible/Infrared Imaging Spectrometer. AVIRIS has 224 bands uniformly sized and spaced from 400 nm to 2500 nm, which largely comprises the visible, near-infrared, and short-wave infrared regions of the electromagnetic spectrum (NASA JPL, 2011). GSD for AVIRIS bands vary as a function of system altitude.

Spectropolarimetric Imaging (SPI)

Spectropolarimetric imaging (SPI) is an emerging technique in the realm of terrestrial remote sensing. It discriminates EM waves on the basis of both wavelength and polarization (Tyo et al., 2006). Spectropolarimetric imaging instruments, like all other remote sensing instruments, can be designed to operate in either an active or a passive fashion.

As the fusion of spectral and polarimetric imaging, spectropolarimetric imaging has utility in most, if not all, of the same fields as its constituent modalities. In cases where either polarimetric or spectral imaging has a significant historical dominance in application, spectropolarimetric imaging provides added dimensionality for decision-making. This is also useful in certain applications where both polarimetric and spectral techniques are already well-characterized, such as target detection (Bartlett et al., 2011). Because they measure polarization angles in multiple spectral bands (Breon et al., 2002), the POLDER instruments mentioned earlier in the chapter are actually spectropolarimetric instruments.

Spectropolarimetric imaging is also valuable in cases where physical interaction with a target is rare, difficult, or impossible, and all light available must be characterized to the fullest extent possible for information about the target. This describes the situation faced by researchers in nearly all planetary and stellar astronomical observations, and explains the popularity of spectropolarimetry as a measurement technique in the astronomical community.

The Opposition Effect

For a variety of materials viewed at a small phase angle—that is, the angle between a light source, the target, and the observer—there is an apparent increase in reflected intensity. This phenomenon is called the opposition effect, or opposition surge, because the direction of the light viewed by the observer is in near or total opposition to that of light from the source (Hapke, Nelson, & Smythe, 1998).

The opposition effect has been observed and studied for decades in planetary astronomy. The effect was first noted by Thomas Gehrels in the 1950s in telescope observations of the asteroid 20 Massalia (Gehrels, 1956). The most popular subject of study regarding the opposition effect, however, has been Earth's moon (Gehrels, Coffeen, & Owings, 1964) (Wolff, 1975) (Hapke, Nelson, & Smythe, 1998) (Hapke, 1986) (Hapke, Nelson, & Smythe, 1993) (Helfenstein, Veverka, & Hillier, 1997). Observations of the Moon as it progresses through its phases show that at the full moon—when the phase angle is smallest for an observer on the Earth's surface, around 4°—the intensity of the light reflected from the Moon's surface is at its peak. Areas of the Moon's surface that are illuminated in the waxing or waning phases appear brighter at the full moon.

The popularity of the Moon as a target for such observations largely arises from the frequency and ease with which it can be observed. Adding to that popularity are the ground truth and material samples collected in the 1960s and 1970s as part of NASA's Apollo program. Astronauts on the surface of the Moon captured a prodigious number of photographs, including many where, with the astronaut's back to the Sun, the opposition effect appears like a halo around the head of the astronaut's shadow, where the phase angle would be smallest. An example image captured by astronaut Harrison “Jack” Schmitt during an extravehicular activity (EVA) during the Apollo 17 mission is shown in Figure 8. A profile of the image intensity values in a horizontal line just above the shadow of the astronaut and below the nearest row of image fiducial crosses—the approximate position of which is indicated by a small arrow on the side of Figure 8—are plotted in Figure 9. The center of the plot in Figure 9 represents the region where phase angle is lowest, and thus has the highest intensity. As one looks increasingly closer to the edge of the image in Figure 8—that is, as the phase angle increases—the corresponding intensity values in the plot in Figure 9 decrease. While an argument can be made that the effect observed in Figure 9 may be due to a vignette effect from the lens system of the camera, sufficient other examples of the phenomenon are available to support the claim that the opposition effect is quite evident in this scene.

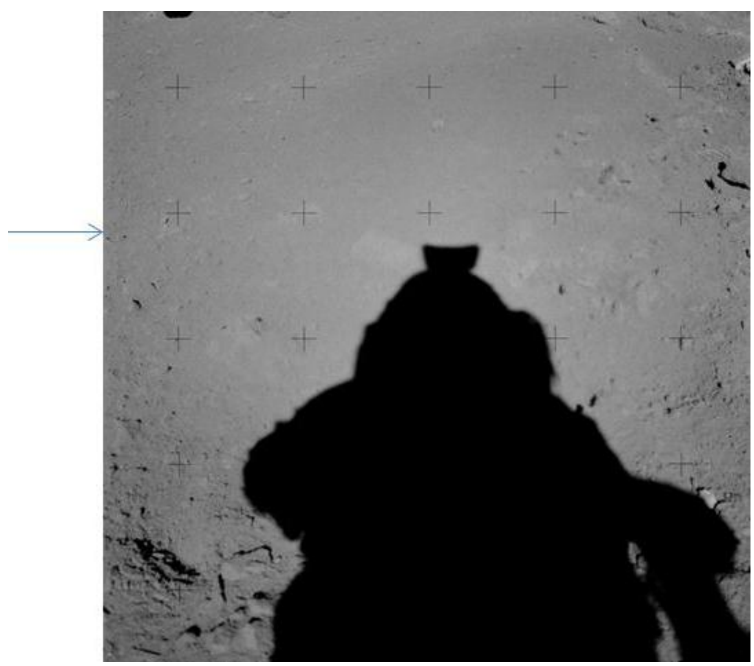

Figure 8 The opposition effect, as photographed by astronaut Harrison Schmitt during an Apollo 17 EVA (NASA, 1972). Arrow indicates general position of horizontal profile in next figure

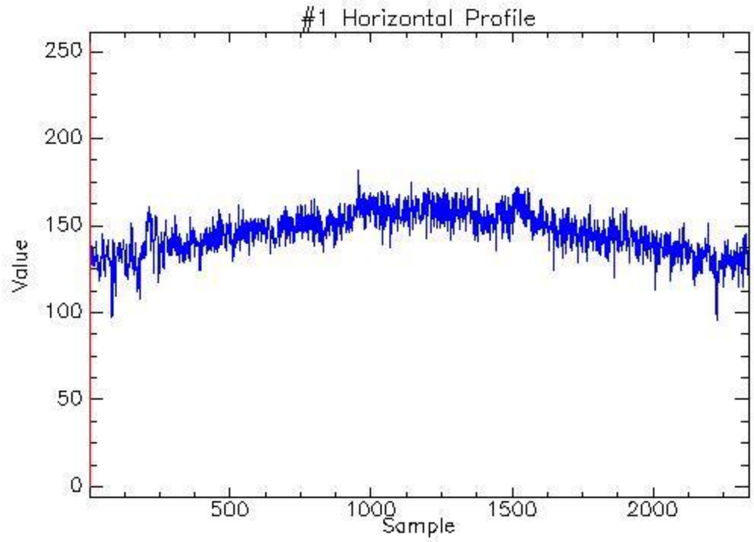

Figure 9 A horizontal profile of image values from the indicated section of Figure 8, showing the opposition effect

While the opposition effect of the Moon is most easily observed at phase angles smaller than 4°, this is often not observable when viewed from the Earth's surface. At diminishingly small (around 1° and less) phase angles an observer on or near the Earth's surface observes a partial or full lunar eclipse, as sunlight that would otherwise be incident upon the Moon is occluded by the Earth (Shkuratov et al., 1999). This is also evidenced in Figure 8, where the part of the scene that would feature a phase angle of zero falls within the shadow cast by the observer. In the case of the Moon, phase angles between 1° and 4° provide sufficient opposition surge for measurement from Earth.

In addition to the photographic and experiential record produced, the Apollo missions returned a large amount of lunar rocks and regolith, permitting many studies at various laboratories around the world. Furthermore, samples of actual lunar regolith allowed for the development of satisfactory simulants, or compounds of similar enough composition and consistency to permit their use in more diverse experiments than might be prudent for the prohibitively rare supply of actual Earthbound lunar regolith (McKay et al., 1994). Spectropolarimetric measurements of both the real and simulated regolith samples exhibit the opposition effect at small phase angle geometries (Shkuratov et al., 2002).

The experience of astronauts living and working on the surface of the Moon revealed that much of the surface is covered in a very fine, powdery basaltic soil, which often jammed hand tools designed for a coarser soil and irrevocably sullied clean white extravehicular suits (Jones, 2001). When undisturbed by all but the natural erosive forces present on the lunar surface—micrometeorite impacts and solar wind—this fine-grained component of the lunar regolith tends to produce microscopic, complex fields of pillar- and tower-like formations and fine-scale layering. During the Apollo program, this came to be known as "fairy castle structure" (Hapke, 2006). Ultimately, observations during Apollo and subsequent laboratory experiments determined that this fairy castle structure has relevance in describing the opposition effect observations of the Moon from Earth.

Shadow Hiding

There are two primary mechanisms that produce the opposition effect. In the first mechanism, known as shadow hiding, the physical bulk of individual or aggregate particles—in the context of lunar regolith, the pillars of the fairy castle structure—cast micro-shadows in the direct sunlight. When the Moon is in a waxing or waning phase, the phase angle for observers on or near the Earth's surface is large, and the aggregate of these micro-shadows on a macro scale produce a certain measurable reflected intensity.

During the full moon, however, the phase angle diminishes to approximately 4°, and the majorities of the micro-shadows cast are occluded by the structure itself; literally, “shadow hiding.” With fewer micro-shadows visible in the macro scale, the reflected intensity is greater (Hapke, 1986). The current consensus in the astronomical community is that shadow hiding is the primary contributor to the opposition effect as observed in measurements of the Moon (Hapke, Nelson, & Smythe, 1998).

Figure 10 depicts shadow hiding. The blue particles are illuminated by a hypothetical light source at some distance above the center of their distribution, in approximately the same location as an observer. All the particles are casting shadows. From the observer’s perspective, the shadows cast by the blue particles in the center of the distribution are not visible, as they are hidden by the particles. To the observer, shadows are increasingly visible with increasing distance—and consequently, increasing phase angle—from the center of the distribution.

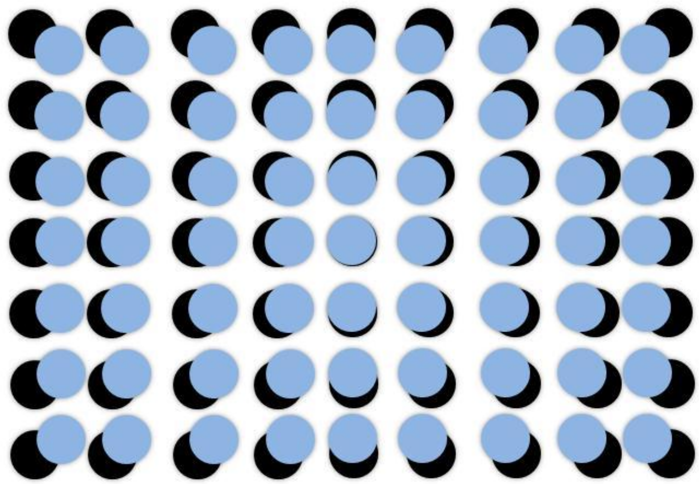

Figure 10 A depiction of shadow hiding; observer and light source are both above center of blue particle distribution

In a shadow hiding scenario, particles are large relative to the wavelengths of light observed. At low phase angle geometries, most of the light reaching the observer has typically gone through only a single scattering event (Hapke et al., 1996). Depending upon the shape of the particles, this may not necessarily impart a strong preferential linear polarization when illuminated by a randomly polarized source (Shkuratov et al., 1999). The polarization is thus also dependent upon the second mechanism by which the opposition effect is produced.

Coherent Backscatter

The second mechanism that produces the opposition effect is called coherent backscatter. It is recognized as a contributing factor to the opposition effect as observed in measurements of the Moon (Hapke, Nelson, & Smythe, 1993) (Hapke, Nelson, &

Smythe, 1998) (Shkuratov et al., 1999). In this mechanism, the wavelength of light incident upon the target material must be approximately the same as the size of the material particles or larger, while the particles must be slightly farther apart than this same size. If the wavelength of incident light is small relative to particle size, then shadow hiding instead of coherent backscatter dominates (Hapke et al., 1992). When the wavelength-particle size relationship conditions are met, the light incident upon the target material is reflected and refracted among many different particles near the material's surface, then ultimately directed back out away from the material. Different waves travel on different scattering paths through the material's particles. When the illumination and observation geometries are similar enough—that is, when the phase angle is small enough—the paths of the waves through the particles are nearly identical, causing constructive and coherent interference and producing increased reflectance at that phase angle geometry. In large phase angle cases this interference does not take place, and only some of the light is scattered in the direction of the observer, interpretable as diminished reflectance (Hapke, Nelson, & Smythe, 1998). Figure 11 shows a coherent backscatter scenario.

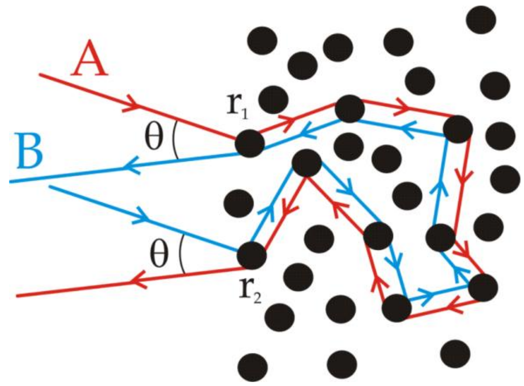

Figure 11 A graphical representation of coherent backscatter (Berto, 2009)

In a scenario like Figure 11, as the number of scattering events increases, the light directed toward the observer is less likely to exhibit a specific polarization preference, and more likely to be randomly polarized. However, due to the relationship between particle size, separation, and other factors, randomly polarized light incident upon the scattering particles will exhibit a preference for linear polarization parallel to the scattering plane as phase angle approaches zero and coherent backscatter is observed (Hapke, Nelson, & Smythe, 1998). This is because light polarized perpendicular to the scattering plane interferes destructively as well as constructively, whereas that which is parallel to the plane only undergoes constructive interference (Shkuratov et al., 1999). In the context of Equation 3, this is a negative polarization feature, a hallmark of the opposition effect.

Research Questions

Spectral or polarimetric measurements alone are not always sufficient for drawing conclusions about the presence or identity of given materials; when combined, however, additional dimensions for characterization are introduced into the decision space. Many researchers involved in remote sensing of the environment already have access to a wide variety of commercial or custom-built spectral sensors. If a widely-used spectral sensor were to be configured with some means of also discriminating incoming light on the basis of polarization, the result would be an improvised spectropolarimeter. Such a sensor would have the potential to allow researchers the opportunity to detect, identify, and characterize materials in situations where previously they might not. Researchers would effectively have two kinds of sensor for the cost of one, plus the cost of the equipment needed for modification; in some cases, this cost is as low as the price of a single photographic filter.

The SOC700 visible and near-infrared (VNIR) hyperspectral imager is one such commercial spectral sensor that is a candidate for conversion into an improvised spectropolarimeter. The SOC700 has an aperture designed to accept a wide variety of optical elements and filters, including polarization filters. The system is portable and may be operated either indoors or outdoors, as long as electrical power is provided and the local environment will not damage the sensor. The SOC700 may be mounted to a tripod, allowing for diverse collection geometries. While the model is no longer manufactured by Surface Optics Corporation, very similar models—notably, the SOC710 and SOC720—are now produced; thus techniques developed and applied with this sensor are adaptable to newer models. Data produced by this sensor can be calibrated into units of radiance or reflectance, and the resulting imagery can be manipulated with any of the popular digital image processing software packages.

Perhaps most importantly, per the manufacturer's specifications, the SOC700 has no inherent sensitivities to polarization; thus, any polarization filter affixed to the front of the camera is the primary discriminator for polarized light detected by the sensor. While it is not uncommon to use a polarization filter on the SOC700, no previous work was found indicating that such a filter was used with the SOC700 to study spectropolarization, instead of mitigating its effects to improve observations of spectral phenomena.

Based on the preceding information, this thesis aims to determine the following:

1. Is it possible to produce a working improvised imaging spectropolarimeter using a SOC700 VNIR hyperspectral imager and a linear polarization filter?
2. Can this sensor observe the opposition effect in various materials?
3. Can the polarization component of the opposition effect be used to detect, discriminate, and/or identify different materials in the visible and near-infrared?

CHAPTER TWO – DATA COLLECTION EQUIPMENT

The SOC700

An improvised spectropolarimeter was created through the addition of a Tiffen 72 mm linear polarization filter to the aperture of a Surface Optics Corporation SOC700 hyperspectral imager. The SOC700 collects data in the VNIR, from 412 nm to 908 nm. It has no inherent sensitivity to polarization.

The SOC700 is comprised of two major components: the camera, and the controlling computer. It can collect imagery both indoors and outdoors, as long as a power source is available to supply electricity to both the camera and its controlling computer. The camera of the SOC700 is approximately 35 cm by 23 cm by 15 cm (approximately 14 inches by 9 inches by 6 inches) in size, and weighs 6.8 kilograms (15 pounds). The optical path uses a scan mirror to direct light from the field of regard into a prism-grating-prism arrangement for decomposition into its spectral components. The camera has a 72 mm aperture with threads for standard photographic optics and filters, and a five degree field of view (Evans, 2007). For laboratory measurements, the camera was alternately set on a countertop or mounted on a tripod. The camera may also be configured to collect in a frame or push-broom mode. For all of the data acquired and reported upon here, the sensor was operated in frame collection mode. A focus wheel on top of the SOC700 camera allows focus adjustment from 2 meters to infinity (Surface Optics Corporation, 2001).

The controlling computer is connected to the camera via a serial cable for sensor operation, and an Ethernet cable for data transmission. Control software and a data capture card are installed in the controlling computer to manage the flow of commands and data to and from the camera. Proprietary Surface Optics Corporation software is loaded on the controlling computer for camera control and configuration, including parameters such as frame vs. push-broom mode, exposure length, scan rate, and sensor gain settings. Dark frames may also be captured for calibration of the data. A processing suite called HSAnalysis2X provides the necessary tools for calibration and format conversion of the HSI data (Surface Optics Corporation, 2001). The controlling computer also has ENVI v4.5 installed. ENVI is an IDL-based digital imaging and remote sensing software suite from Exelis VIS. Other versions of ENVI used on other systems in this study are v4.8 and v5.0.

Figure 12 is an annotated image of the SOC700 and its supporting equipment in the laboratory, as it was configured for this study.

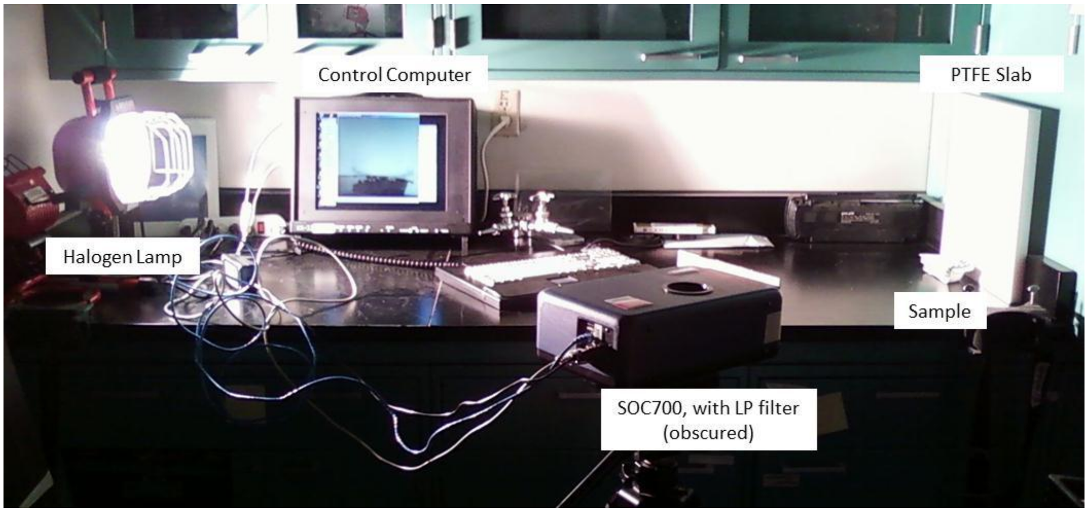

Figure 12 An annotated image of the SOC700 and associated equipment configured for spectropolarimetric measurements

In frame mode, the SOC700 produces 120-band HSI cubes. Each band is a 640 sample by 640 line image. The raw, uncalibrated data are written in band sequential order and as 16-bit integers, yielding files that are each approximately 94 MB in size. Using the HSAnalysis2X software, dark frames can be subtracted from the data to reduce sensor noise influence, and factory-measured calibration response curves are applied to convert the data from raw digital counts to units of radiance (specifically, milliwatts per square centimeter steradian nanometer, or $mW/cm^2 \cdot sr \cdot nm$). If a white reference is present in the scene at time of imaging, it can then be used to set a white point for the image and convert the cube to reflectance.

The output file size of a floating point reflectance cube generated in HSAnalysis2X is approximately 187 MB. Prior to post-processing in ENVI, a header file must be generated for each image file to allow correct reading of the file.

The Linear Polarization Filter

A Tiffen 72 mm linear polarization photographic filter was attached to the front of the SOC700 to allow discrimination of linear polarization angles. This filter is created by a thin polarizing film layered between two optical glass. Dual filter cross-polarization extinction—the orientation of two such filters orthogonal to one another to determine the percentage of light transmitted—is approximately 2% (The Tiffen Company, 2012). A visible transmittance spectrum for a similar linear polarization filter is shown in Figure 13.

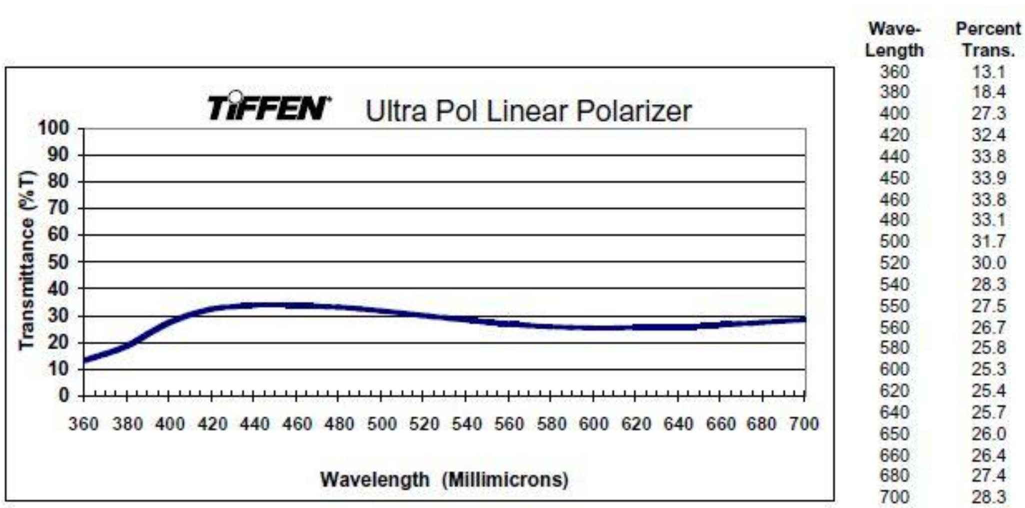

Wave-Length	Percent Trans.
360	13.1
380	18.4
400	27.3
420	32.4
440	33.8
450	33.9
460	33.8
480	33.1
500	31.7
520	30.0
540	28.3
550	27.5
560	26.7
580	25.8
600	25.3
620	25.4
640	25.7
650	26.0
660	26.4
680	27.4
700	28.3

Figure 13 Transmittance spectrum for Tiffen Ultra Pol linear polarization filter, similar to that employed (The Tiffen Company, 2012)

The photographic filter does not have any markings to indicate the transmissive axis. This was determined empirically through observation through the filter of an illuminated surface. The illumination angle met the Brewster's angle condition; i.e., the reflection off the surface was linearly polarized at a specific angle. The linear polarization filter was rotated to find the orientations for which the reflection was most visible and least visible; from these observations, the transmission axis was determined and marked on the edge of the filter with white paint. Measurements at different polarization angles required rotation of the linear polarization filter by hand.

Reference angles to assist orientation of the linear polarization filter were marked on the camera via a card that had been lined with a protractor. This card was then affixed to the front of the SOC700 camera and aligned with a mark taped to the camera body, to assist in reproducibility of setup between collection events. Four different linear polarization angles are indicated on the card: 0°, 45°, 90°, and 135°. These angles were intentionally selected, and are described as the modified Pickering method for characterizing the polarization state of light (Schott, 2009). The angles were selected for their relative ease of use in post-collection processing (see Chapter Four). An image of the card in place on the front of the SOC700 camera is shown in Figure 14; in the image, the alignment arrows are clearly visible on the left.

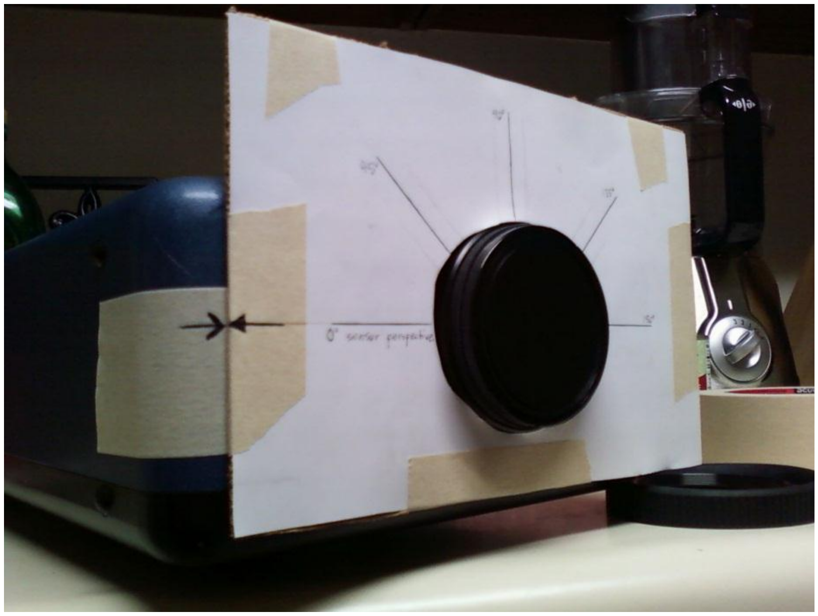

Figure 14 The polarization angle card, affixed to the front of the SOC700 camera

A review of the literature on opposition effect measurements of various materials with both broad- and narrow-spectrum light sources indicates that a circularly polarized component as well as a linearly polarized component can be measured at small phase angle geometries (Hapke et al., 1992) (Hapke, Nelson, & Smythe, 1998). However, measurements were not performed with a circular polarization filter for several reasons. First, polarization filters were selected on the basis of affordability. This prompted filter selection from consumer photography suppliers, not an uncommon tactic for researchers designing small sensors. While many affordable circular polarization filters are available, during the period of equipment procurement no practical method by which such a filter could be determined to be passing left-hand or right-hand circular polarization was identified. Distinction between chiralities is critical for characterizing the circular polarization state of light. Second, the use of an improvised circular polarization filter created through the addition of a quarter wave plate (described in Chapter One) was deemed impractical for two reasons: the cost of a quarter wave plate was prohibitively expensive, and the use of a quarter wave plate would have negated the broad-spectrum measurement capabilities of the SOC700 (as a quarter wave plate is only truly such at a specific wavelength, and thus only helps produce and measure circular polarization at a certain wavelength). Third, the vast majority of polarimetric and spectropolarimetric imaging systems referenced in terrestrial remote sensing literature use of linear polarization angles exclusively; while references to systems measuring circular polarization exist, they are not nearly as numerous (Schott, 2009) (Tyo et al., 2006). This includes laboratory instruments dedicated to observations of the opposition effect (Shkuratov et al., 2008). Developing the improvised imaging spectropolarimeter with linear polarization in mind helps guarantee the sensor can be repurposed toward applications other than opposition effect spectropolarimetry, should it be desired.

Illumination Sources

Measurements were performed using a Husky 700 W halogen work lamp as an illumination source. This lamp employs two bulbs to produce the indicated power: one at 500 W, and another at 200 W. Both bulbs were illuminated simultaneously during measurements. These linear bulbs are parallel to one another in the lamp, which surrounds the bulbs with a large reflector to direct the light outward. The lamp face is a flat piece of transparent glass, which filters ultraviolet (UV) light as a safety measure. This filtration of light from the source is assumed to have no impact upon measurements.

The lamp face is also covered by a grill, which is also assumed to have no influence. The halogen lamp is shown in Figure 15.

Figure 15 The halogen lamp

The halogen lamp was characterized as producing randomly polarized light. The lamp was activated and viewed through two linear polarization filters, which were placed one in front of the other and rotated through a full 360° relative to the observer, while being kept at fixed angles relative to each other. The filters were first oriented at the same angle, then orthogonally, to determine if there were any variations in observed intensity of light being transmitted as both filters were rotated. The lack of any variation in intensity during rotation indicated a lack of preference for any particular linear polarization angle in the light emitted from the source; thus, the light from the source was confirmed to be randomly polarized.

Some early measurements were performed outdoors in sunlight. The Sun and the halogen lamp are similar in that their spectra are relatively broad and cover the full spectral range of the SOC700, even though the spectra are not identical. The Sun was determined to be an impractical light source for the opposition effect spectropolarimetric measurements. The continuously varying solar illumination geometries and skyshine from clouded or unclouded sky change at too rapid a rate for reliable use with this system.

The standard illumination source of the laboratory is a series of fluorescent light strips hanging from the ceiling. Early laboratory measurements used both the halogen lamp and room lights, but this approach was rapidly discarded; spectra of the fluorescent lamps could not be sufficiently calibrated out of the scene, and interfered with the analysis of the spectra of the target materials. All measurements were performed again with the fluorescent lights off, using the two bulbs of the halogen lamp as the sole source of illumination.

White Reference

A square slab of polytetrafluoroethylene, or PTFE, served as a white reference. The slab is approximately 0.45 meters by 0.45 meters by 0.02 meters (approximately 18 inches by 18 inches by 1 inch) in size. PTFE has a diverse array of applications, and in the remote sensing community is most popularly referred to by the trade name Spectralon. PTFE is frequently the material of choice in scientific applications as a white reference for calibration to reflectance. Spectralon is considered a good approximation of a Lambertian surface, which diffusely reflects incident light in a uniform distribution (Goldstein, Chenault, & Pezzaniti, 1999).

The PTFE slab was placed behind the sample container, presenting the broad side of the slab in the direction of the halogen light source; it remained stationary throughout all the laboratory measurements.

Both the slab and a small round disk of calibrated Spectralon were loaned by the National Institute of Standards and Technology (NIST). This calibrated disk, a NIST White Diffuser SRM 2044 (serial number 2044a-01-7), was used to characterize the slab and confirm that it was suitably similar in reflectance for use in measurements. The slab was preferred for use over the disk because the slab was easier to keep stationary, and was less inclined to be accidentally moved or adjusted when changing samples between measurements.

The PTFE slab does exhibit some degree of polarized reflectance depending on the angle of incidence of light on its surface. The strength of the polarization of light reflected from the slab increases as the angle of incidence (relative to the surface normal) increases. Goldstein, Chenault, and Pezzaniti have shown that doped Spectralon, used to provide references with lower reflectance percentages, produce higher degrees of polarization. High percentage reflectance Spectralon, similar to the slab, was found to have a small degree of polarization in the spectral and angular ranges used for this study (Goldstein, Chenault, & Pezzaniti, 1999). The effect was small enough to be deemed negligible in this study.

Sample Containers

For the final series of laboratory measurements, Dixie white paper bowls were radially bisected, allowing a view of the interior of the bowl in profile. The paper bowls were printed in some places with blue and green floral print; this was used as a cursory check of the function of the SOC700 during measurements and post-processing, to confirm that the sensor was producing reasonable spectral results. Samples were placed within the half-bowl while inside the fume hood of the laboratory to minimize dust escape during material manipulation. One half-bowl was used for each material sample. Half-bowls were numbered with a pen to help keep track of material identities during collection events.

Goniometry

Goniometry is the measurement of angles between objects. In the context of opposition effect studies, goniometry involves measurement of the phase angle. Laboratory measurements of the opposition effect involve the use of goniometers, instruments capable of measuring very fine angles (Shkuratov et al., 2008). Phase angle for this study was calculated trigonometrically from measurements of distance between the lamp, the sensor aperture, and the sample container.

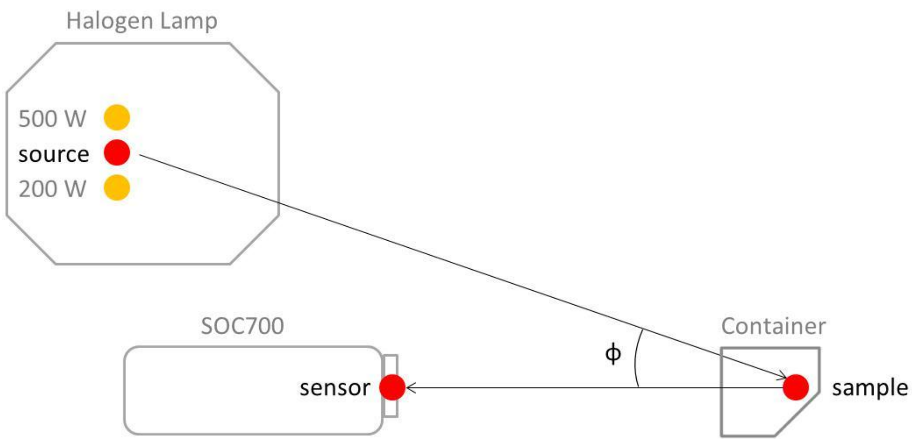

Figure 16 Diagram of setup in cutaway profile, showing key measurement points in red (not to scale)

A single point between the two bulbs of the halogen lamp was used to represent the light source for distance measurements. For the sensor, the reference point was the center of the aperture of the SOC700. For the sample, the reference point was the back wall of the sample container. Figure 16 is a diagram illustrating these key measurement points.

Operating Conditions

Initial proof-of-concept measurements testing the operation of the sensor were carried out at several outdoor locations in the Northern Virginia region in late 2009. Locations included the George Mason University Fairfax Campus in Fairfax, Virginia, and Bluemont Vineyard in Bluemont, Virginia. Opposition effect materials measurements using the sensor were ultimately made indoors under controlled artificial lighting discussed earlier. Table 1 presents a summary list of all collections. Dates on which data shown in this study were collected are marked with an asterisk. Table 2 provides a breakdown of collection parameters for the asterisk-marked series from Table 1.

Table 1 Record of collections with SOC700 as improvised imaging spectropolarimeter (asterisk denotes collection dates covered in analysis)

Date	Location	Environment	Conditions	Objectives
14 November 2009	GMU Campus, Fairfax, VA	Outside (parking lots, campus pond)	Overcast w/ intermittent rain, cool temps.	System test and initial collections
15 November 2009	Bluemont Vineyard, Bluemont, VA	Outside (rural)	Mostly clear, moderate temps.	System test and initial collections
18 November 2009	Fairfax, VA	Outside (residential)	Overcast, cool temps.	Assorted collections
10 October 2011	Centreville, VA	Outside (residential)	Mostly clear, moderate temps.	Outdoor opposition effect meas. Test
5, 7, 8 November 2011	GMU Campus, Fairfax, VA	Laboratory	Room temp.	Lab opposition effect meas. Test
17 December 2011	GMU Campus, Fairfax, VA	Laboratory	Room temp.	Lighting test
8 January 2012	GMU Campus, Fairfax, VA	Laboratory	Room temp.	Metal oxides, rare earth oxides tests; exposures lengthened
3 March 2012*	GMU Campus, Fairfax, VA	Laboratory	Room temp.	New filter & white ref., exposures lengthened, final materials start
31 March 2012*	GMU Campus, Fairfax, VA	Laboratory	Room temp.	Final materials end

Table 2 Record of collection series, detailing system setup for each event (asterisk denotes collection dates covered in analysis)

Date	Environment	Filters	Light Source	White Ref.	Sample Container	Exposure Length
3 March 2012*	Laboratory	Skylight 1B, 72 mm Tiffen LP	700W halogen	PTFE slab	Half-bowl	0.030 s
31 March 2012*	Laboratory	Skylight 1B, 72 mm Tiffen LP	700W halogen	PTFE slab	Half-bowl	0.030 s

CHAPTER THREE – TARGET MATERIALS AND MEASUREMENTS

A variety of granular materials with varying particle sizes and spectral profiles were measured. Three factors drove material selection: spectral characteristics, applications, and availability. Table 3 provides identification information for the materials.

Table 3 Record of materials measured

Material Name	Product Name	Source	Chemical Formula (if available)	Lot No.	Notes
baby powder	Johnson's Baby Powder	Purchased	-	2291RB	-
concrete	RapidSet Professional Grade Concrete Mix	Purchased	-	433022812	-
Ductal	Lafarge Ductal	Donated by colleague	-	JS1000RS	Ultra-high performance concrete
molybdenum VI oxide	N/A	Lab stock (SAIC)	MoO_3	Stock #36687, Lot # I20G05	CAS# 1313-27-5; ACS 99.5% min (assay)
neodymium oxide	N/A	Donated by colleague (MITRE)	Nd_2O_3	-	-
potassium nitrate	Spectracide Stump Remover	Purchased	KNO_3	LOT-02071-B	Powdered via electric grinder
praseodymium III, IV oxide	N/A	Lab stock (SAIC)	Pr_6O_{11}	Stock # 11234, Lot # A28D14	REacton 99.9% (REO)

Material Name	Product Name	Source	Chemical Formula (if available)	Lot No.	Notes
Salt	Morton Salt w/o iodide	Purchased	$NaCl$	17A2AA10	-
Sand	Garden Pro Paver All Purpose Sand	Purchased	-	-	Damp when purchased in November 2011; dry by January 2012
sodium metabisulfite	Bonide Stump-Out	Purchased	$Na_2S_2O_5$	11063001	Not powdered via electric grinder
titanium II oxide	N/A	Lab stock (SAIC)	TiO	Stock # 77126, Lot # F24H09	99.5% (metals basis)
titanium III oxide	N/A	Lab stock (SAIC)	Ti_2O_3	Stock # 77127, Lot # J28G17	99.8% (metals basis)
titanium IV oxide	N/A	Lab stock (SAIC)	TiO_2	Stock # 36199, Lot # B03H31	Anatase; 99.9% (metals basis)
vanadium V oxide	N/A	Lab stock (SAIC)	V_2O_5	Stock # 11094, Lot # P2594	99.8% (assay)

Spectral characteristics divided the materials into two main groups: spectrally similar, and spectrally unique. The spectrally similar materials were all white in appearance, implying a relatively high reflectance value across the visible spectrum. Given this similarity, such materials were deemed to be ideal for determining whether an opposition effect polarization component could provide enough uniqueness between the materials to aid in their distinction.

The materials comprising the spectrally unique group each possessed a unique VNIR spectrum. They were selected to determine whether an opposition effect polarization component could provide additional characterization information for these materials. The group was comprised of several metal oxides and rare earth oxides, as well as paving sand.

The application of a material was also a critical factor in its selection. Ductal, manufactured by Lafarge, is an ultra-high performance concrete (UHPC). It contains sand and cement, like regular concrete, but also contains pure powdered quartz, reinforcing metals, and fiber elements to produce a material that can withstand compression at higher pressures than traditional concrete (Smart concrete, 2012). Ductal is increasingly being used not only for civil projects such as dams and sewer pipes in earthquake-prone regions, but for producing hardened military facilities such as bunkers. Several countries are actively pursuing the study and implementation of UHPC in both civil and military applications, making the ability to distinguish between traditional and ultra-high performance concretes relevant to Western defense organizations (Smart concrete, 2012). A sample of regular commercial concrete was also measured for comparison.

Sodium metabisulfite and potassium nitrate are common tree stump removers, which have merit in remote sensing studies for forestry applications. Additionally, the potassium nitrate-based stump remover, when ground to smaller particles as this sample was, can be combined with charcoal and sulfur to produce black powder (Gurstelle, 2009). Sodium metabisulfite, however, cannot. The purchase of sodium metabisulfite-based stump removers by would-be bomb makers seeking to procure a source of potassium nitrate is a common mistake. Both materials have a white powdery or granular appearance in their off-the-shelf product form.

Figure 17 provides a visual grouping of the selection criteria for the materials described above, while Figure 18 shows pure samples of the materials, annotated with their names.

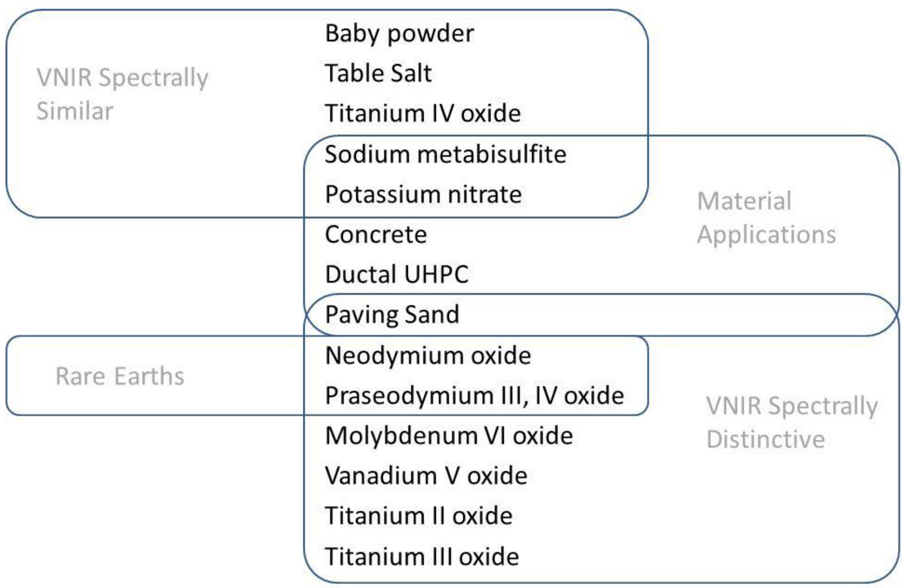

Figure 17 A visual grouping of the materials studied, grouped by characteristics of interest

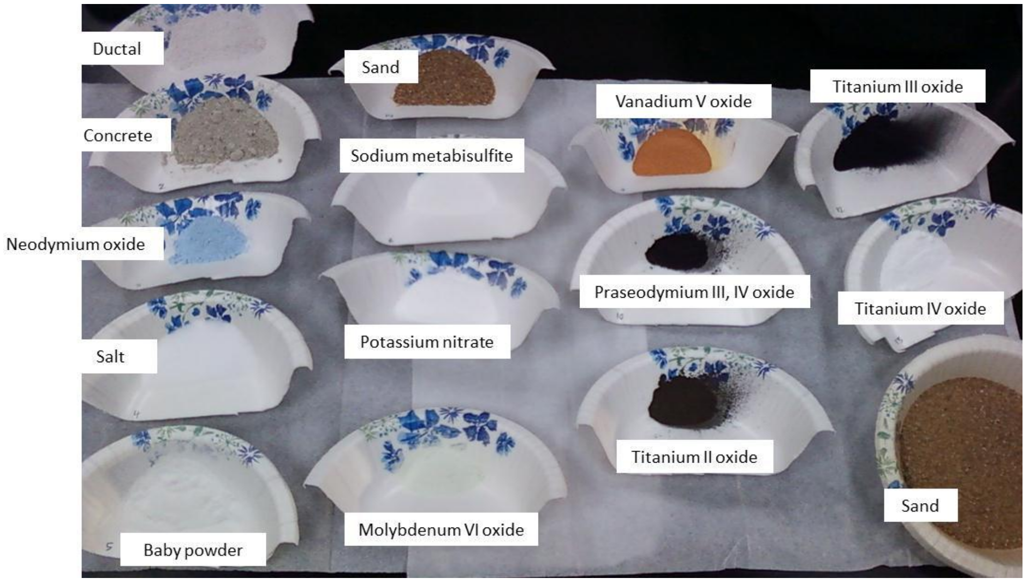

Figure 18 Annotated image of pure material samples

SPI collections for both pure and sand-mixed samples were performed. Pure material samples were poured, not tamped, into the sample containers. Sand-mixed sample preparation involved mechanically mixing the sand with the target until the best possible uniformity had been achieved, as determined via visual inspection. The sand-to-material mixture ratio was approximately one-to-one by volume. Final measurements involved sifting the sand prior to measurement and mixing; this was done to remove overly large pebbles and stones that otherwise took up too large an area in the scene. Mixing sometimes produced clumps of non-sand material; when these could not be sufficiently reduced, pixel sampling in post-processing was directed toward non-clump regions of mixture. Mixing coarse sand with certain fine-particle materials also often yielded mixtures that would striate with only slight motion of the sample container. Figure 19 shows an annotated image of the sand-mixed materials.

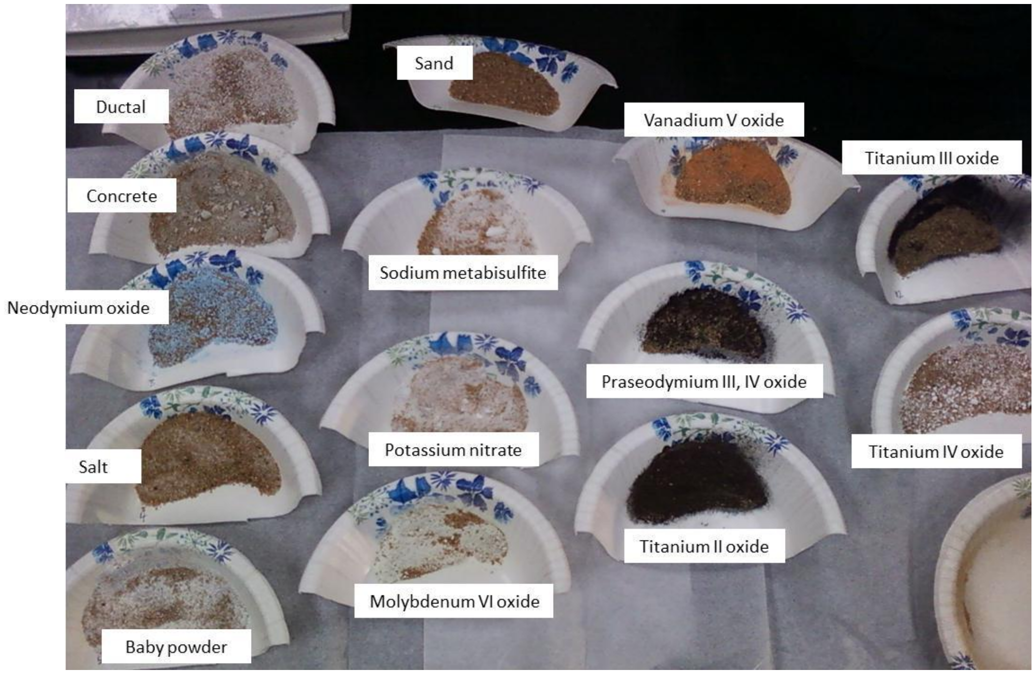

Figure 19 Annotated image of sand-mixed material samples

Materials in the sample containers typically presented a sloped surface toward the light source and sensor. No attempts were made to measure or characterize the three-dimensional surface geometry of the materials.

Measurement Technique

The most significant improvement throughout the collection campaign was the development and application of techniques for keeping the sensor from moving between measurements. As shall be discussed in Chapter Four, image-to-image registration between measurements of the same scene with varying linear polarization angles is critical for producing useful spectropolarimetric products.

Several different tripods were used for sensor positioning and stabilization. A consumer grade photographic tripod was found to be too weak to reliably hold the sensor, which caused issues with image-to-image registration. This tripod was replaced with a stronger, heavier, professional grade tripod, which provided a stable mount for the sensor. When not on the tripod, the sensor was placed flat on a countertop in the laboratory instead. In both the tripod and countertop configurations, any instances in which the camera was perceptibly and accidentally moved during or in between collections for a specific material prompted a re-measurement of all cubes of the material at that geometry, to assure the best possible image-to-image registration.

Switching the camera between filtered and unfiltered configurations yielded an exposure issue that was eventually resolved. The SOC700 control software automatically adjusts the apparent dynamic range displayed on screen, which is representative of the values written to file when a cube is saved by the user. Setting the exposure length when the linear polarization filter was in place and performing measurements, then removing the filter often yielded drastically overexposed imagery, while the opposite—setting exposure length with the filter removed, making measurements, then replacing the filter—yielded very underexposed imagery. The solution was to reset the exposure length of the camera to the same value each time when removing or replacing the filter, then collecting a test cube to force the SOC700 control software to adjust the dynamic range appropriately. When employing this solution, the sensor’s scan mirror occasionally covered a smaller angle than normal; repeated test cube collection alleviated this issue as well.

Typical distance between the front of the sensor and the approximate center of the target material ranged between approximately 0.5 to 1.7 meters. While the minimum focal distance for the SOC700 camera is 2 meters, as described in Chapter Two, these distances were forced by the working environment. Even at these shorter-than-optimal distances, however, using the documented technique of adjusting the focus wheel produced in-focus SPI data (Surface Optics Corporation, 2001).

CHAPTER FOUR – DATA PROCESSING

Conversion of Raw Data to Reflectance

After collection, raw data cubes are converted to floating point reflectance cubes. There is one cube for each linear polarization angle measured at each phase angle, as well as at least one unfiltered cube collected at a small phase angle. All cubes are converted to reflectance within HSAnalysis2X.

The process of converting the original files from raw digital counts to reflectance values begins with a dark correction. The dark frame collected at the start of measurements is subtracted from the raw data; this has the effect of flat-fielding the data through the removal of any dark current artifacts that may have been recorded during dark frame collection, where the sensor's only source of detected energy is itself.

Once the dark correction is complete, a factory-provided sensor response curve is applied to convert datasets to units of radiance (milliwatts per centimeter squared steradian per nanometer, or $mW/cm^2 \cdot sr \cdot nm$). The SOC700 has four calibration files: two each for high and low gain, with each gain having separate files for the presence or absence of a polarization filter on the sensor. Unfortunately, the specific kind of polarization filter used for the calibration file is unknown. The "low gain, polarization" calibration file was used for the conversion to radiance for all datasets collected with the Tiffen polarization filter in place. Reference cubes collected without the linear polarization filter in place on the sensor were processed using the “low gain, no polarization” calibration file.

The third step in conversion to reflectance is the setting of the dataset’s white point, also known as a white or light correction. A region of interest is selected over the white reference within the scene using the HSAnalysis2X software, and an average spectrum saved to a text file. White reference region selections are chosen to be as close as possible in position, and thus illumination geometry, to the sample. This text file is then accessed by HSAnalysis2X, where it is used as the denominator for a ratio calculated for every pixel in the scene. As the white reference is (correctly) assumed to be the brightest object in the scene—though not so bright as to saturate the detector—all pixels in the ratio scene that do not represent the white reference thus have a reflectance value between zero and one. The pixels for the white reference itself have values at or near unity.

Generation of Stokes Imagery Products

Reflectance files are used as inputs for batch processing routines to generate Stokes imagery products. The batch processing routines are written in the IDL programming language and use components of ENVI.

The Stokes imagery products are the result of band math operations performed on the reflectance cubes, determining the differences in reflectance at different linear polarization angles at a particular spot in the scene. Excellent image registration (typically, an error of less than one pixel) between different cubes is required for satisfactory results. Consequently, only the linear polarization filter is adjusted while collecting imagery for a specific material; the sensor is not moved until all polarization angles have been collected.

Stokes imagery products derive from the Stokes vector, which is not a true vector in the mathematical sense but a construct that contains parameters that completely describe the polarization state of a given quantity of light. The Stokes vector is presented in Equation 4. The Stokes parameters were first introduced in the mid-19th century by George Stokes, a British mathematician and physicist (Schott, 2009). Several different taxonomies exist to identify the different parameters; two are shown in Equation 4, but only the S-number convention (i.e., S_0, S_1, S_2, S_3) is subsequently used.

Equation 4 The Stokes Vector, which contains four parameters

$$S = \begin{bmatrix} I \\ Q \\ U \\ V \end{bmatrix} = \begin{bmatrix} S_0 \\ S_1 \\ S_2 \\ S_3 \end{bmatrix}$$

Equation 5 The S_0 Parameter, per the modified Pickering method

$$S_0 = \frac{I_0 + I_{45} + I_{90} + I_{135}}{2}$$

Equation 6 The S_1 Parameter, per the modified Pickering method

$$S_1 = I_0 - I_{90}$$

Equation 7 The S_2 Parameter, per the modified Pickering method

$$S_2 = I_{45} - I_{135}$$

Equation 8 The S_3 Parameter

$$S_3 = I_R - I_L$$

The S_0 parameter represents the total intensity of the light in the scene regardless of the intensity *I* measured for a particular polarization angle or chirality; the parameter is described in Equation 4. A spectral plot from an S_0 image cube appears similar to that from a hyperspectral cube. The S_1 parameter represents the difference between horizontally and vertically polarized light, and is presented in Equation 6. The S_2 parameter represents the difference between two different diagonal polarization angles, and is presented in Equation 7. The S_3 parameter represents the difference between the two different chiralities of circularly polarized light, and is presented in Equation 8 (Tyo et al., 2006).

Together, Equation 5 through Equation 8 fully represent the polarization state of light. As shown in the equations, the Stokes parameters pertaining to linear polarization—S_0, S_1, and S_2—are computed from the measurement of intensity at four different linear polarization angles: 0°, 45°, 90°, and 135°. Measuring this set of linear polarization angles for assessing the polarization state of light is referred to as the modified Pickering method. This method does not include measurements of circular polarization. There are options beyond these four angles for performing the same task; in fact, S_0, S_1, and S_2 can be computed from three linear polarization angles—0°, 60°, and 120°—in a measurement approach called the Fessenkov method (Schott, 2009). This approach would require alteration of Equation 5 through Equation 7; in fact, these equations can be altered to represent the measurement of any number of linear polarization angles, though lower numbers tend to be more practical to measure. The modified Pickering method was selected due to its widespread use. The orthogonal relationship between the linear polarization angles increases the suitability for opposition effect measurements, particularly when considering the $I_{\perp}$ and $I_{\parallel}$ distinctions made in reference to the scattering plane in relationship to Equation 3.

Measurement of Spectra, and Additional Processing

Once all Stokes image products have been generated, the images are displayed in ENVI and linked together, so that any particular region selected for one of the images is selected for all. An 11x11 pixel sample region is selected centered on the target material's location in the image, and an average spectrum for the region is computed. An 11x11 pixel region is used for two reasons. The averaging mitigates system noise impacts to the spectral information. The number of pixels in the region is sufficient to meet traditional statistical requirements (i.e., there are more than thirty samples in the average). Spectra are then compared with one another.

Principal Components Analysis (PCA)

Principal components analysis (PCA), a technique commonly applied to hyperspectral imagery for data analysis, was applied to a subset of the SPI cubes. Briefly, each band of an HSI or SPI cube can be considered as a single axis, each orthogonal to the others. The value of a pixel in a certain spectral band is that pixel's position along that band's axis, so that the total spectral content of the pixel serves as a coordinate for the pixel's position within N-space, where N is the number of spectral bands. The principal components transformation is a coordinate transform, which produces a new set of axes to minimize the amount of correlation in the data (Richards & Jia, 2006). When producing an output image cube, the result of a principal components transformation has the same number of bands as the input cube. Each pixel from the original cube now has coordinates in the transformed space, and consequently a new spectrum.

Lower order bands in a principal components transform output cube have the least amount of correlation. When calculating principal components transforms in ENVI, a plot of principal component eigenvalues is also produced. This plot demonstrates how the variance of the data is distributed across the bands, which are presented as eigenvalue numbers. A plot that rapidly diminishes asymptotically to near-zero indicates a dataset that has low data variance in the original spectral space.

CHAPTER FIVE – ANALYSIS, RESULTS, AND DISCUSSION

Stokes image products were analyzed and spectra from all products were plotted for comparison. Analyses were applied to address the research questions posed in Chapter One.

Does the sensor work?

The combination of the SOC700 and the linear polarization filter indeed produces a working improvised imaging spectropolarimeter.

Spectropolarimetric imagery collected in the laboratory included portions of the black countertop surface on which the materials rested. Two factors from Chapter One, then, are immediately relevant in the observed behavior for this dark, flat surface: Brewster's angle, and the Umov effect.

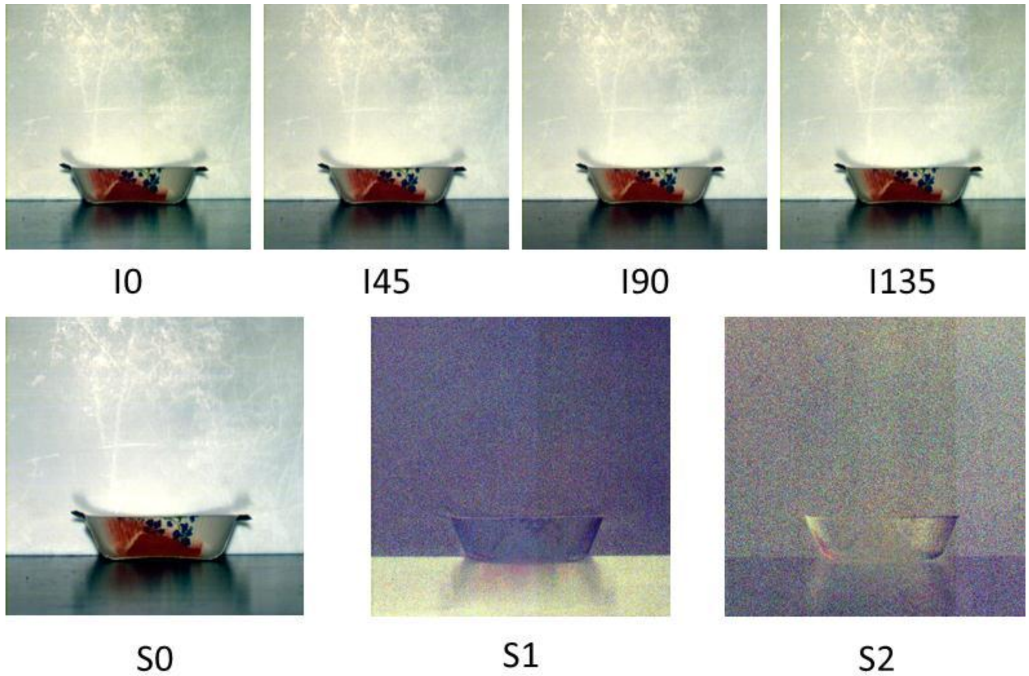

Figure 20 Intensity images (top four) and Stokes parameter images (bottom three) for pure vanadium V oxide sample at a phase angle of ~4°, 3 March 2012. Color assignments are R: 701 nm (band 72), G: 536 nm (band 32), B: 436 nm (band 7).

Figure 20 above provides images of the four input intensity images—each collected at a different linear polarization angle, as indicated by their *I*-number label—and the resulting output Stokes parameter imagery for measurements of pure vanadium V oxide, from the group of spectrally diverse materials. Phase angle for this series of images is approximately 4°.

The angle between the camera and the normal of the countertop surface in the immediate vicinity of the material sample is very high, approximately 87°. This indicates the sensor is in the optimal orientation for measurements of the countertop within the constraints of Brewster's angle, as was previously described in Chapter One. Recall that

Brewster's angle is the angle below which reflectances are strongly polarized parallel to the surface. There is no requirement for a forward-scattering geometry to be in place for Brewster's angle conditions to hold true; thus, the backscattering conditions for opposition effect measurements can also satisfy Brewster's angle polarization observation conditions. Thus, the countertop should be expected to produce strong horizontal polarization, and thus a dominant S_1 value, and brightness for those parts of the image representing the countertop surface in the S_1 image. This is evident in Figure 20, with a bright countertop in the S_1 image, and a dark countertop in the S_2 image. The Umov effect and the dark color of the countertop also support a strong polarization component measureable for the surface.

Is the opposition effect observable?

The sensor is able to observe the opposition effect. This is based upon analysis of results for measurements of neodymium oxide, the material for which the most diverse set of phase angles were collected. S_0 spectra for a pure sample of this material, collected at varying phase angle geometries, are shown in Figure 21. These S_0 spectra are themselves sampled at three different wavelengths, in areas where the spectra have distinct similarities or distinctions, and plotted as a function of phase angle in Figure 22.

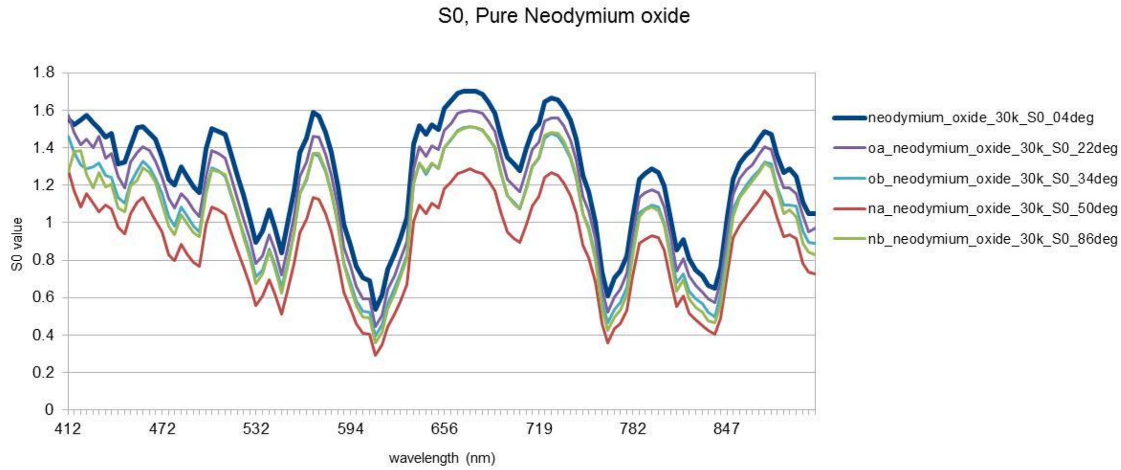

Figure 21 Plot of S_0 values for pure neodymium oxide, measured at different phase angles

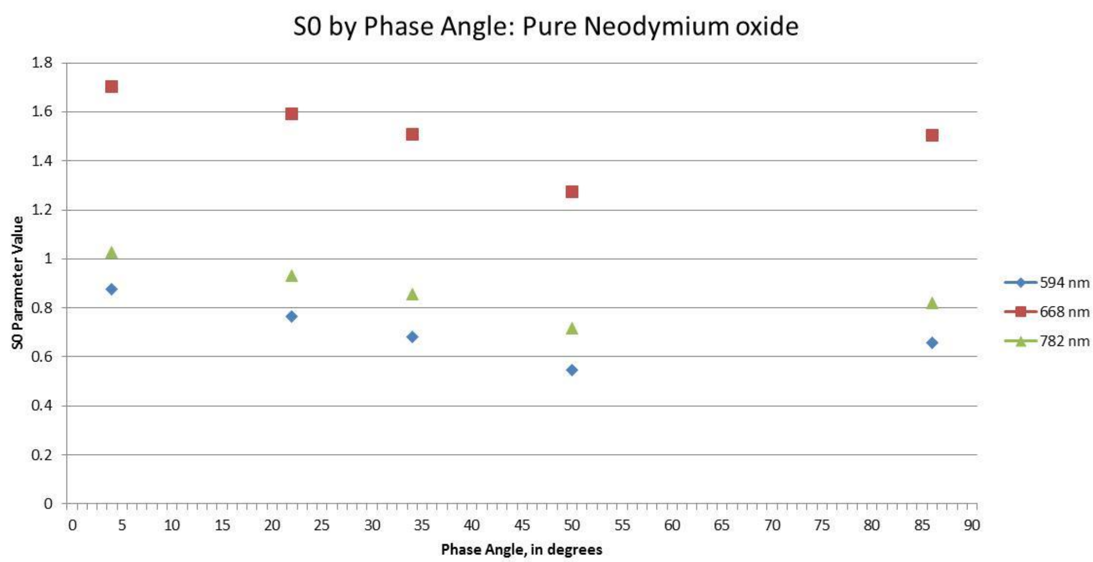

Figure 22 Plot of S_0 values as a function of phase angle for pure neodymium oxide, sampled at three different wavelengths

Figure 22 is a plot of S_0 as a function of phase angle for pure neodymium oxide for three wavelengths. It shows that at low phase angles, the material is exhibiting its highest measured intensity. The sensor is likely detecting the opposition effect for the pure neodymium oxide.

Measurements at the 86° phase angle are higher in S_0 value than some of the intermediate phase angle values. This result is not unexpected, as at such a high phase angle the material is being observed in the transitory region between backward-scattering and forward-scattering, the latter of which may often have higher reflected intensities than non-opposition effect cases of the former.

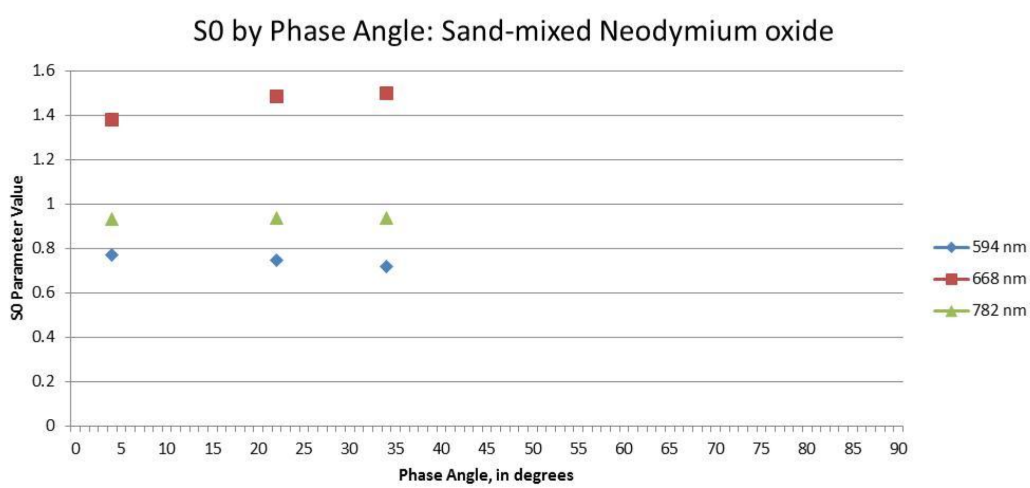

Figure 23 Plot of S_0 values as a function of phase angle for sand-mixed neodymium oxide, sampled at three different wavelengths

Figure 23 is a plot of S_0 values as a function of phase angle for the sand-neodymium oxide mixture, sampled at the same three wavelengths as Figure 20. It is immediately apparent that the opposition effect is not observed.

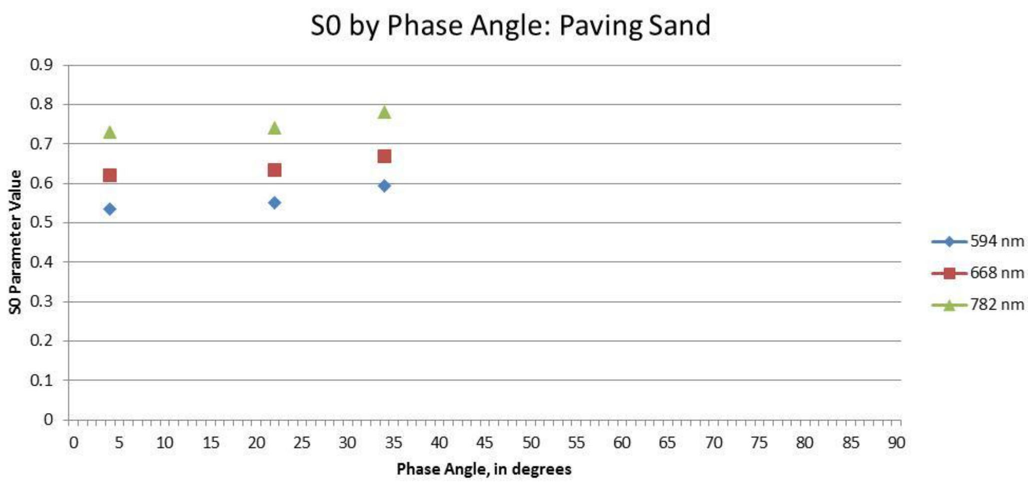

Figure 24 Plot of S_0 values as a function of phase angle for paving sand, sampled at three different wavelengths

The opposition effect is not observed because the large particle size of the sand relative to the wavelengths observed, the primary mechanism for any opposition effect observations would be shadow hiding. It is likely that the size distribution and arrangement of sand particles do not have enough structure to produce sufficient shadows to make the effect easily observable, and thus the dominant factor in the results observed for the sand-mixed neodymium oxide and pure sand is not the opposition effect but solely that of spectral reflectance.

Does opposition effect SPI aid in material discrimination?

Spectra from the Stokes parameter imagery indicate the possibility that opposition effect spectropolarimetry aids material discrimination in the VNIR. The spectra for both the S_1 and S_2 imagery, already averaged from a sample of 121 pixels, are very small-valued (typically under ±0.02) and noisy. Invariably, both the pure and sand-mixed S_2 samples were near-zero valued throughout the entire spectral range of the sensor, yielding little information. Thus, the following discussion focuses solely upon the S_1 results from imagery collected at a 4° phase angle for pure and sand-mixed cases. Each of the four material groups are considered.

VNIR Spectrally Similar Materials

The group of materials spectrally similar in the VNIR was comprised of baby powder, table salt, titanium IV oxide, sodium metabisulfite, and potassium nitrate. To varying extents, from approximately 600 to 700 nm each pure material exhibited a negative S_1 value—that is, a preference for vertical polarization—at a phase angle of 4°. The S_1 spectra for these pure materials are plotted below in Figure 25.

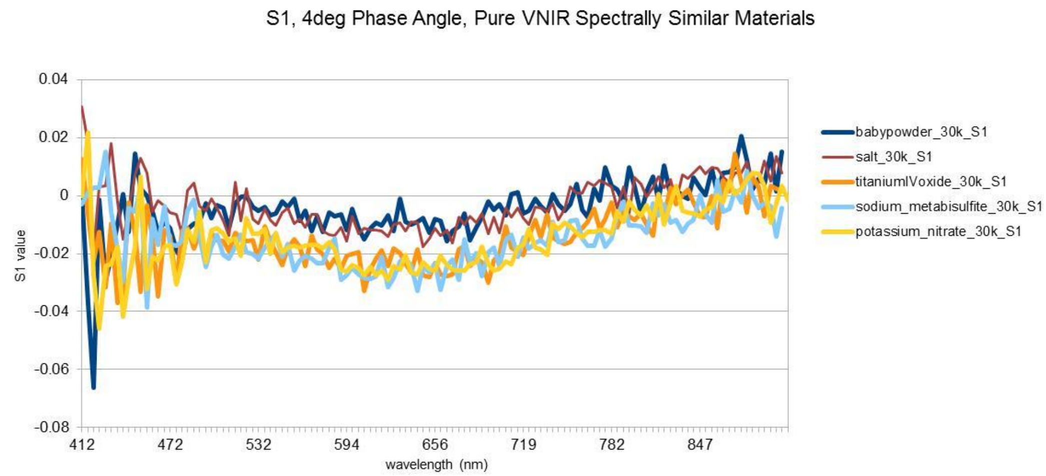

Figure 25 S_1 spectra for spectrally similar pure materials at 4° phase angle

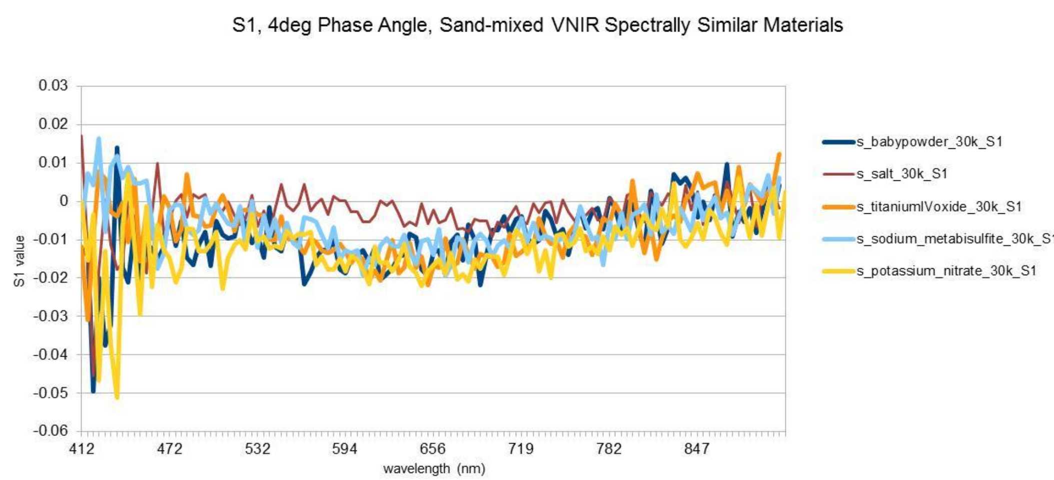

Figure 26 S_1 spectra for spectrally similar sand-mixed materials at 4° phase angle

Figure 26 above is a plot of S_1 spectra for the same materials mixed with sand. It is similar to the results of the pure materials in Figure 25 in that the same "smile" shape peaking around 650 nm is retained; however, the smile is less pronounced for the sand-mixed salt than the pure salt, and more pronounced for the sand-mixed baby powder than the pure baby powder.

VNIR Spectrally Distinctive Materials

The group of spectrally distinctive materials in the VNIR was comprised of paving sand, neodymium oxide, praseodymium III, IV oxide, molybdenum VI oxide, vanadium V oxide, titanium II oxide, and titanium III oxide. There is no unifying trend for the materials in this group with respect to behavior in the S_1 parameter; as seen below in Figure 27, different materials stay near zero in value, slightly positive and thus in preference to horizontal polarization, or slightly negative and thus in preference to vertical polarization around 600 to 700 nm, like the spectrally similar materials.

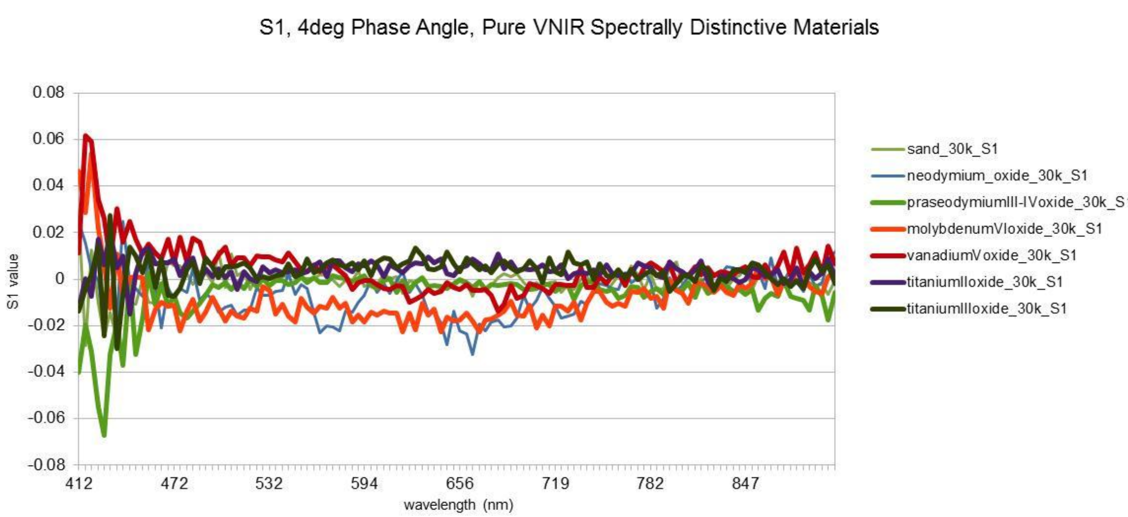

Figure 27 S_1 spectra for spectrally distinctive pure materials at 4° phase angle

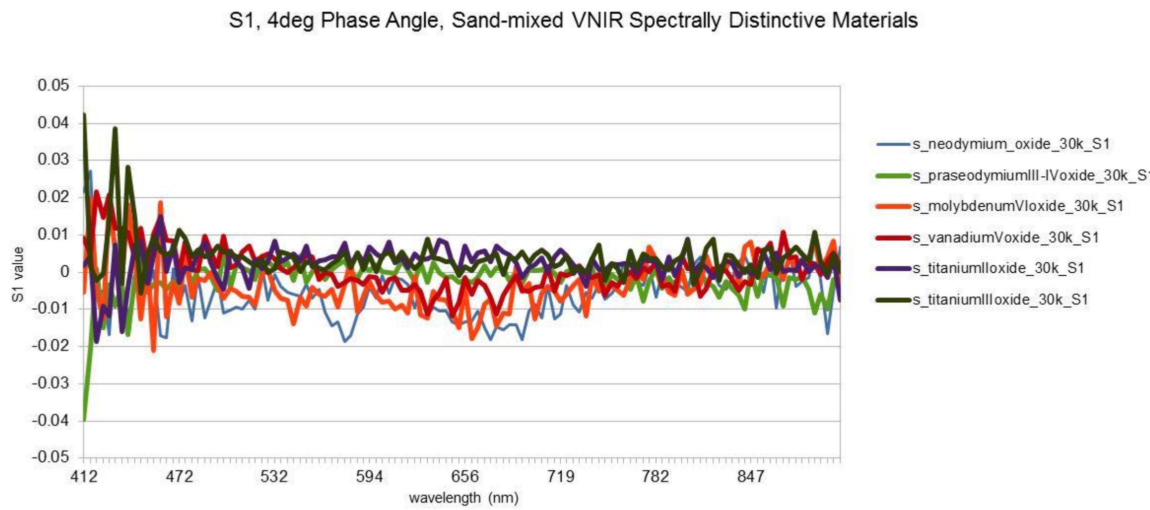

Figure 28 S_1 spectra for spectrally distinctive sand-mixed materials at 4° phase angle

Figure 28 above is a plot of the S_1 spectra for the same materials at the same 4° phase angle, mixed with sand. The curve for sand has been removed. The negative S_1 values for molybdenum VI oxide and neodymium oxide have reduced in magnitude, and in general all values are closer to zero for the sand mixed samples than the pure samples.

Rare Earth Oxides

The subset of spectrally distinctive materials that comprises the rare earth oxide grouping contains neodymium oxide and praseodymium III, IV oxide. The S_1 spectra of these materials at a 4° phase angle are shown in Figure 29.

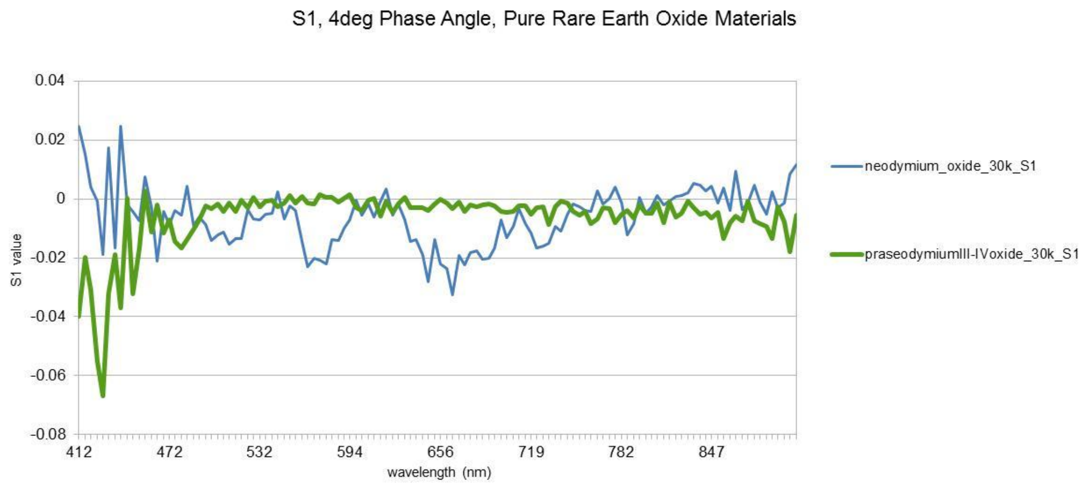

Figure 29 S_1 spectra for pure rare earth oxides at 4° phase angle

The S_1 spectra for praseodymium III, IV oxide are almost uniformly zero in the central spectral range of the sensor, while that of the neodymium oxide is extremely variable on the scale presented. This is an intriguing result, and a unique one out of all the materials measured. Initial review prompted questions about misregistration between the 0° and 90° linear polarization intensity images, which in the S_1 band math calculation would lead to incorrect results. The registration was exonerated through further analysis. Additionally, the S_1 image does not exhibit any of the hallmark visual indications of misregistration, specifically dark and light edges on opposite sides of an object, typically in the horizontal dimension when the sensor is resting on the countertop and has no significant elevation angle component. A comparison between the neodymium oxide S_1 image and an example misregistered S_1 image from earlier laboratory measurements is presented in Figure 30. The neodymium oxide S_0 image is included as a reference.

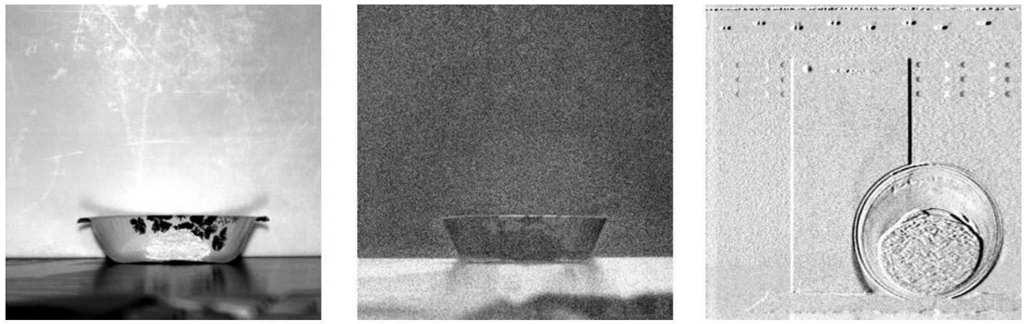

Figure 30 From left to right: neodymium oxide S_0 image; neodymium oxide S_1 image; example S_1 image of pure baby powder from earlier lab measurements, with known misregistration of input intensity images. All images showing band 63, 664 nm

In Figure 30, the baby powder S_1 image clearly exhibits the opposing black and white edging from misregistration of the input intensity images. The S_1 image for the pure neodymium oxide sample does not.

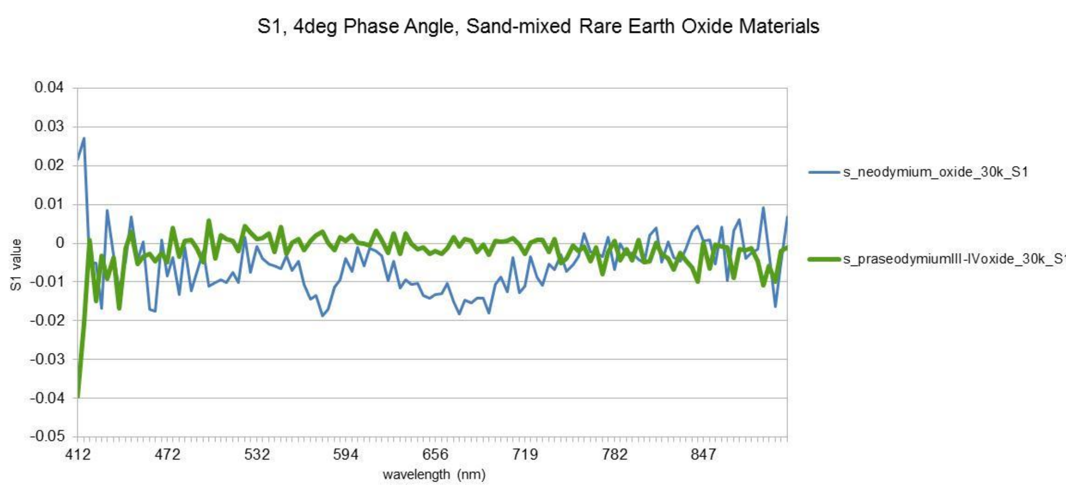

Figure 31 S_1 spectra for sand-mixed rare earth oxides at 4° phase angle

Figure 31 is a plot of the S_1 spectra for the sand-mixed rare earth oxides. Compared to the spectra of pure samples in Figure 29, there is little to no change in the state of values for sand-mixed praseodymium III, IV oxide. The magnitudes of values for sand-mixed neodymium oxide are approximately half those of the pure samples, but the general features remain the same.

Applied Materials

The applied materials group includes materials that are both spectrally similar and spectrally distinctive in the VNIR. Materials included are sodium metabisulfite, potassium nitrate, concrete, Ductal UHPC, and paving sand. The S_1 spectra for pure samples of these materials at a 4° phase angle are presented in Figure 32.

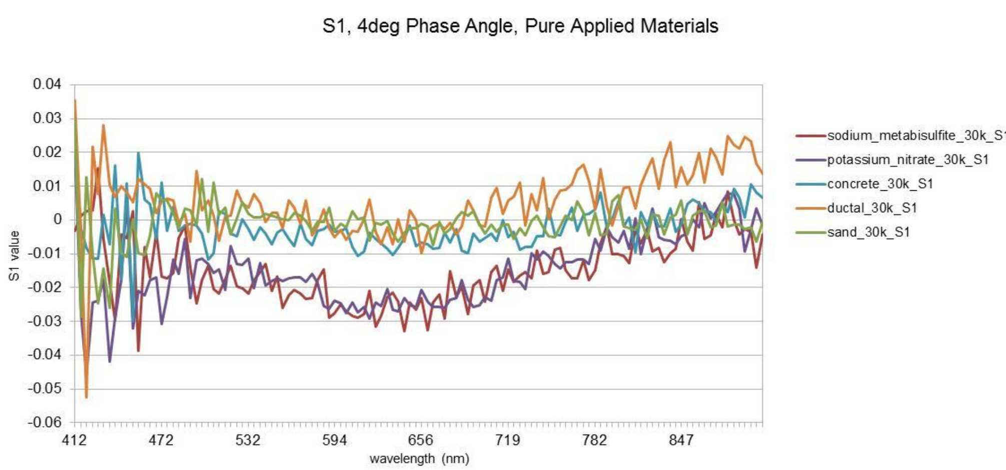

Figure 32 S_1 spectra for pure applied materials at 4° phase angle

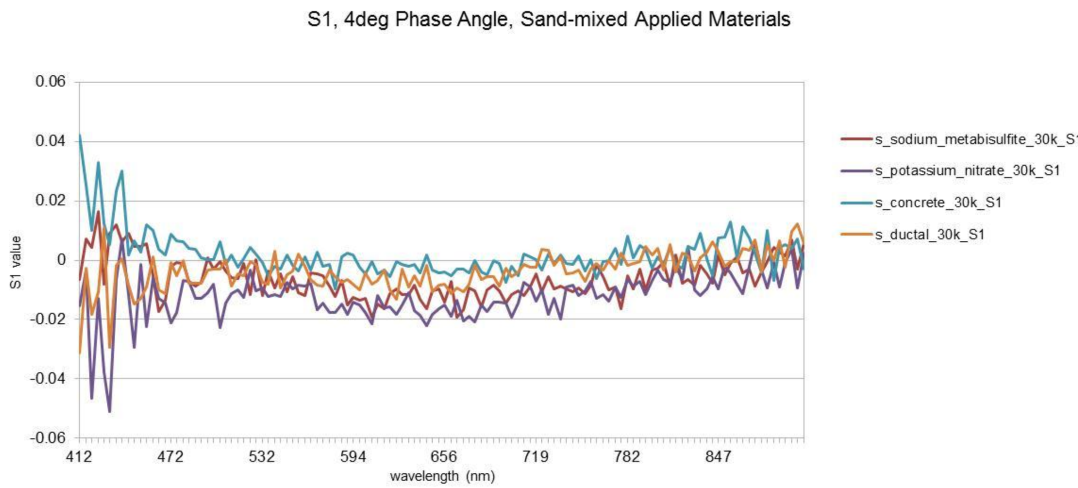

Figure 33 S_1 spectra for sand-mixed applied materials at 4° phase angle

Figure 33 above plots the S_1 spectra for sand-mixed samples of the applied materials. As with Figure 28, the curve for sand has been removed. There is little change in the curve for concrete, while the S_1 values for Ductal in the longer red and near-infrared wavelengths are closer to zero for the sand-mixed sample than the pure sample, for which values were distinctly positive. The smile shape of the S_1 spectra for sodium metabisulfite and potassium nitrate, clear in the pure sample spectra, are flattened in the sand-mixed samples.

Noise in S_1 and S_2 Spectra

The S_1 spectra shown are all extremely small-valued and noisy, as are the S_2 spectra (not shown). There are several possible explanations.

One possibility is that the exposure was insufficient. Almeida (1995) shows that the signal-to-noise ratio (SNR) for the S_1 and S_2 parameters is less than the square root of the number of detected photons; if there is insufficient light of any polarization reaching the sensor from the target, the signal of light with a specific polarization may not be distinguishable from sensor noise. While the number of photons detected by the sensor is unknown, observations of the countertop—described earlier as having a strong positive S_1 value—indicate sufficient exposure. Additionally, initial laboratory measurements included test collections at different exposure lengths and source power to determine optimal illumination conditions.

Another possibility is that all of the materials produce weak polarization at best. This is supported through inspection of eigenvalues from PCA results for the S_1 and S_2 images. A representative example is the eigenvalue plot for the S_1 image of pure neodymium oxide, shown in Figure 34 with the first two bands of the PCA product. The brightest area in the first PCA band is the countertop; the sample container can be identified in front of the PTFE, and the neodymium oxide is barely visible within. In the second PCA band, the boundary between the PTFE and the countertop is visible through heavy noise. The outline of the sample container is barely resolved; its contents are not resolved at all. The plot of eigenvalues for the PCA product show an initial sharp decrease as eigenvalue number increases from 1 to approximately 10, then asymptotically approaching zero over all higher eigenvalue (PCA band) numbers. The implication is that the S_1 image contains little polarization information beyond that observed from the countertop.

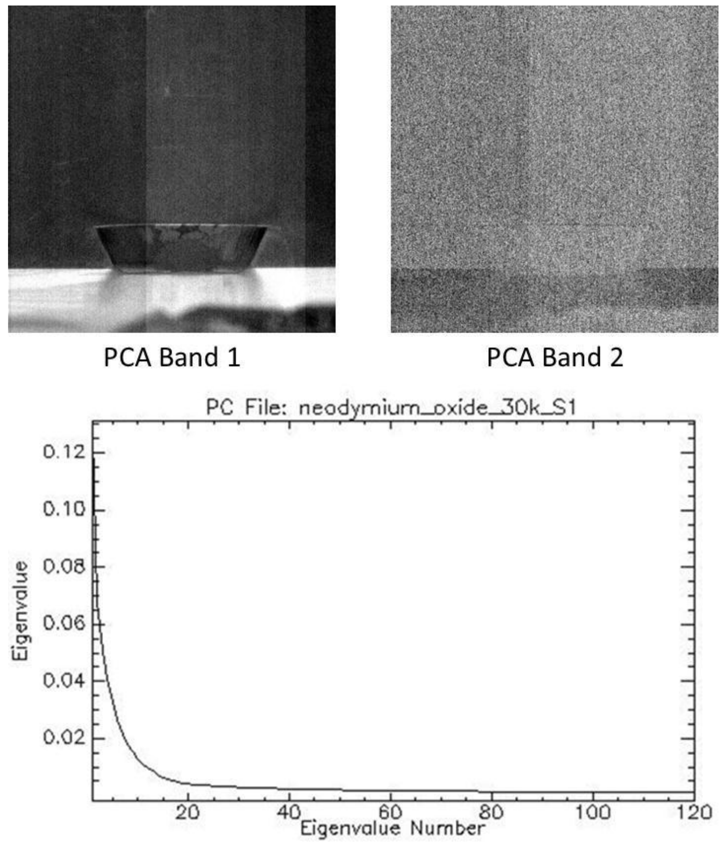

Figure 34 Top: first and second band images from PCA product calculated from a pure neodymium oxide S_1 image. Bottom: eigenvalues calculated for the same S_1 image

Because the polarization from the target is so weak, there is little difference in the values of the various intensity images (I_0, I_{45}, I_{90}, and I_{135}). This yields small values for S_1 and S_2. Although the exposure is sufficient, Almeida's remarks on SNR remain relevant, as the S_1 and S_2 calculations are carried out on more noise than signal. The PCA band images of Figure 34 show non-uniform response across the scene, suggesting as a third possibility that the noise characteristics of this SOC700 may make it unsuitable for measuring weak polarimetric signatures. At small phase angles, it is possible that the heat of the halogen lamp, in close proximity to the SOC700, introduces or increases a thermal noise component as well.

CHAPTER SIX – FUTURE IMPROVEMENTS AND RESEARCH

Operation of the sensor provided many opportunities to identify potential improvements to the equipment and techniques employed, as well as potential applications for spectropolarimetric imaging in general.

Reducing Noise

The noise in the S_1 and S_2 spectra, as seen throughout Chapter Five, is a significant issue. A series of hardware and processing approaches are offered to mitigate this noise.

No maintenance record is available for the SOC700, and it is possible that the camera is due for tuning and recalibration; annual recalibration at the factory is recommended (Hendricks, 2012).

No information is readily available regarding the type and quality of the polarization filter used to generate the calibration files for the SOC700. It is possible that the factory filter and the Tiffen linear polarization filter employed are different enough to cause disparities in the data; however, this is not very likely.

An additional technique that may improve the noise qualities of the Stokes parameter spectra is the application of a smoothing filter. The Savitzky-Golay filter is a least-squares polynomial filtering technique developed in the 1960s that is often used to reduce noise in spectra while retaining spectrally-significant moments. As is often the case with digital filters, changing the width of the filter applied can modify the impact on the data; in one configuration the filter is “weak” and retains more of the shape of the spectrum, while in another the signal-to-noise ratio (SNR) for a known spectral feature is increased (Bromba & Ziegler, 1981). The application of a Savitzky-Golay filter in the weak mode would assist in determining natural features, if any, of the Stokes parameter spectra generated from the sensor’s output.

System Improvements

In general, use of the sensor for future studies that require a high degree of polarimetric fidelity should likely be preceded by an extensive examination of error propagation, such as the approach of Boger et al. in their analysis of the behavior of a similar imaging spectropolarimeter (Boger et al., 2003). In their approach, an instrument model is constructed and constantly updated as various instrument errors and their propagation through the full system are characterized, and ultimately used to improve the instrument. This approach is appealing because it focuses on iterative updates of error sources, and avoids attempting to predictively model all possible error sources.

Improvements to system goniometry are recommended. Post-collection trigonometric calculation of phase angle is sufficient for some applications of SPI, and these same methods can be used in setup for approximate sensor positioning, as employed here; however, techniques such as opposition effect spectropolarimetry are better served by fine control over phase angle. An actual goniometer would be appropriate.

Furthermore, increases to the phase angle in this study involved the movement of the sensor outside of the original scattering plane. This creates a new scattering plane that is tilted respective to the original, which obfuscates comparisons of $I_{\perp}$ and $I_{\parallel}$ (from Equation 3) between collections at different geometries. Future measurements should endeavor to maintain a single scattering plane for collections at all phase angles.

Sensor Improvements

The most obvious improvement to the design of the sensor is to decrease the amount of time required to perform collection of all required linear polarization angles. In the conditions used for the study, the shortest exposure length used for each line of the detector array was 0.03 seconds per line; scan time for 640 lines is approximately 20 seconds. When added to time required for filter adjustments and data management, this yields a time of anywhere between 30 and 60 seconds, at a minimum, to collect a single spectral cube at a particular linear polarization angle. When collecting multiple linear polarization angles at multiple geometries for multiple pure and mixed samples, the amount of time required for collections adds up quickly.

Recent designs of imaging spectropolarimeters increasingly incorporate gigabit Ethernet cameras (Bartlett et al., 2011) and specialty filtering methods (Gupta et al., 2000) (Anchutkin et al., 2008) (Escuti et al., 2006) (Aharon et al., 2008). Acousto-optical tunable filters (AOTFs) and photoelastic modulators (PEMs) rely upon changes in the refractive index of an optical material under strain mechanically induced to produce standing waves in different patterns. These patterns are similar to a wire grid polarizer; however, the patterns are variable depending upon the action of the transducers creating them, thus producing “tunable” filters capable of producing variable linear polarization angles at controlled high frequencies (Glenar et al., 1994) (Diner et al., 2007). Liquid crystal tunable filters (LCTF) are also rapidly adjustable to various linear polarization angles, and allow faster measurements (Aharon et al., 2008). Reactive mesogen filters are similar to LCTFs in that they also use liquid crystals; however, elements of these filters are static after filter creation (Escuti et al., 2006). In the case of each advanced filter method, the angles are reproduced more rapidly or accurately than manual rotation of a filter, as with the improvised SOC700-based sensor. When combined with gigabit Ethernet cameras or even purpose-built spectrometers, these filters allow faster imagery collection than the SOC700.

An alternate high-speed collection approach is to employ imaging Fourier transform spectrometers designed for sensitivity to polarization, creating Fourier transform spectropolarimeters (Craven et al., 2010). Sensors like these are often designed for channeled spectropolarimetry, which is an SPI technique that uses a combination of optical retarders and polarizing elements to produce a waveform that can be frequency filtered to return spectrally-resolved Stokes parameters, collected instantly and simultaneously (Taniguchi et al., 2006). Fourier transform spectrometers also maintain better signal-to-noise ratios than dispersive systems like the SOC700 (Craven et al., 2010), suggesting the possibility of Stokes parameter spectra with less noise than that observed in this study.

Light Source Improvements

Though the broad VNIR spectrum of the halogen lamp was ideal, the dual-bulb design of the lamp is non-optimal. Many laboratory measurements of the opposition effect use light sources that are distant or small relative to their targets, often acting as suitable point source approximations. For the sizes and separation of the bulbs at the relatively close sample distance employed in the final laboratory measurements of this study—2 meters or less—the point source approximation is invalid. The separation of the bulbs likely diminished any potential influence of the shadow hiding mechanism, with the shadow cast by particles illuminated by one bulb reduced or eliminated by illumination from the other. The 500 W bulb alone, or both bulbs used together with an integrating sphere possessing a single small aperture, would be preferable for future use.

Further exploration of opposition effect spectropolarimetry may require a polarized light source. This can be achieved through certain laser source designs or with a broad-spectrum source such as a halogen lamp illuminating solely through a polarization filter.

Processing Improvements

Several additional improvements in processing are recommended to increase product creation rates. These include automation of conversion to reflectance, automated extraction of spectra from the resulting products, and calculation of additional products.

The conversion to reflectance, described in Chapter Four, is a manual process. The HSAnalysis2X software does not have a batch processing mode, meaning that the user must manually perform dark subtraction, radiance calibration, and setting the white point for each dataset. An automated process for the completion of this task, similar to that for the batch processing of Stokes parameter imagery, would significantly reduce the amount of time required for completion. This process could be combined with the Stokes parameter batch processes, as well as automation for spectral sampling afterward, to produce an efficient method for analysis of SPI data collected by the sensor.

Additional products, such as degree of linear polarization (DOLP), can be created from available data. DOLP is useful for determining how much linear polarization may actually exist in a scene in a general sense, and not at any specific linear polarization angle. It is an extension of the more generalized equation for degree of polarization (DOP), which contains the S_3 parameter for circular polarization; when calculating DOP for cases in which circular polarization is negligible, or for sensors that do not measure circular polarization, DOP and DOLP are equivalent (Tyo et al., 2006).

Additional Applications of the Sensor

The sensor is suitable for a number of different applications that feature static or slow-changing environments, allowing time for sufficient exposure length and polarization filter rotation. One example is vegetation studies. Woessner and Hapke performed *in vivo* studies on the polarization of light scattered at different VNIR wavelengths by healthy and distressed Dutch clover, *trifolium repens*. They observed not only the Umov effect, but also correlations between leaf reflectance and geometry and polarization that can feasibly be used to remotely study vegetative health over a broad area (Woessner & Hapke, 1987).

Water is an appealing but difficult target. Homma et al. (2005) performed collections of water samples using an LCTF-based VNIR spectropolarimeter. However, imaging only took place after the water surface in the sample containers had calmed, which is not always reliable outside of a laboratory environment. Ottaviani et al. (2008) performed glint characterization using a polarimeter mounted on a rail suspended above a wave tank, illuminating with a 635 nm laser through a linear polarization filter. In both cases, the sensors employed sampling much more quickly than the SOC700. Tonizzo et al. (2009) take the unusual approach of performing VNIR spectropolarimetric collections underwater, measuring chlorophyll and mineral concentrations. The SOC700 is not a suitable sensor for comparable activities, as it cannot be immersed in water without significant specialized protective equipment.

A possible application suitable for a SOC700-based spectropolarimeter is monitoring and identifying chemicals in water at treatment and purification facilities. Water samples could be placed into shallow pans and evaporated, leaving behind solids for observation. Automated collection and comparison against a pre-generated spectropolarimetric library would allow remote monitoring of water quality at the facility, assuming the chemicals in question posessed distinctive spectral features in the VNIR.

Moving SPI Deeper into the Infrared

An extensive literature exists on spectral studies of many terrestrial phenomena in the VNIR. Spectropolarimetric studies in this regime are catching up rapidly. New spectropolarimetric challenges await in the short-wave, mid-wave and long-wave infrared, or SWIR, MWIR, and LWIR, respectively. At these wavelengths—1.4 to 3 microns for SWIR, 3 to 8 microns for MWIR, and 8 to 15 microns for LWIR—most terrestrial targets are more emissive than reflective, and the polarization state becomes a function of the temperature and surface geometry of the observed target (Schott, 2009). This can lead to new and exciting applications, such as the modeling of an object based on a single passive collection, as compared to the active generation of a point cloud or interferometric pattern as with lidar or radar. Experiments have also been performed in shadow penetration, where vehicles parked in the shade of a tree line were undetectable in the VNIR and unpolarized LWIR, but detectable using polarized LWIR (Tyo et al., 2006). Additional experiments and simulations have been carried out in mine and tripwire detection (Forssell, 2001) and in discriminating between reentry vehicles and balloon decoys for ballistic missile defense (Pesses et al., 2002).

CHAPTER SEVEN - CONCLUSION

Spectropolarimetry is an established astronomical measurement technique that is experiencing a surge of interest in the terrestrial remote sensing community. To this end, an existing spectral imaging system sensitive in the VNIR was outfitted with a linear polarization filter, creating an improvised imaging spectropolarimeter. Three questions were posed regarding the sensor and its data.

First, would the sensor produce valid spectropolarimetric results? This was confirmed through reflectance measurements of a dark, flat countertop surface. Production of Stokes parameter imagery from these observations confirmed a strong horizontally polarized reflection from the surface.

Second, could the sensor be used to observe the opposition effect, a phenomenon of various materials in which there is an increase in reflected intensity at phase angles of 4° and less? S_0 measurements of pure neodymium oxide, a spectrally distinctive rare earth oxide, at three different wavelengths and various phase angles ranging from 4° to nearly 90° indicate successful observation of the opposition effect.

Third, could the polarization component of the opposition effect be used to aid material discrimination? S_1 and S_2 spectra for the materials showed slight distinctions between materials, but were small-valued and extremely noisy; this suggests promise for the technique in general, but that this particular sensor may not be suitable for the task.

Various improvements for the sensor are offered: processing improvements for noise reduction and efficiency, illumination improvements for geometry control, and a discussion on how to collect measurements faster using different collection methods. Potential applications in the VNIR and longer infrared wavelengths are discussed.

REFERENCES

REFERENCES

Smart concrete. (2012, March 3). *The Economist*, pp. 89-90.

Aharon, O., Safrani, A., Moses, R., & Abdulhalim, I. (2008). Liquid crystal tunable filters and polarization controllers for biomedical optical imaging. *Proceedings of SPIE, 7050*.

Almeida, J. S. (1995). Uncertainties in the determination of the Stokes parameters due to photon noise. *Astronomy & Astrophysics Supplement Series, 109*, 417-423.

Anchutkin, V. S., Belsky, A. B., Voloshinov, V. B., & Yushkov, K. B. (2008). Hyperspectral optical system with spatial separation of images possessing different polarization direction. *Proceedings of SPIE, 7100*.

Barta, A., Horvath, G., Bernath, B., & Meyer-Rochow, V. B. (2003, January 20). Imaging polarimetry of the rainbow. *Applied Optics, 42*(3), 399-405.

Bartlett, B. D., Schlamm, A., Salvaggio, C., & Messinger, D. W. (2011). Anomaly detection of man-made objects using spectro-polarimetric imagery. (S. S. Shen, & P. E. Lewis, Eds.) *Proceedings of SPIE, 8048*.

Berto, J. (2009, July 3). *File:Coherent backscattering.png.* Retrieved May 2012, from Wikimedia Commons: http://commons.wikimedia.org/wiki/File:Coherent_backscattering.png

Blackburn, D. G., Buratti, B. J., & Ulrich, R. (2011). A bolometric Bond albedo map of Iapetus: Observations from Cassini VIMS and ISS and Voyager ISS. *Icarus, 212*, 329-338.

Boger, J. K., Stokes, S. D., Bowers, D. L., Ratliff, B. M., & Fetrow, M. P. (2003). An error evaluation template for use with imaging spectro-polarimeters. *Proceedings of SPIE, 5158*, 113-124.

Boutet, E. (2007, May 14). *File:Onde electromagnetique.svg.* Retrieved May 2012, from Wikimedia Commons: http://commons.wikimedia.org/wiki/File:Onde_electromagnetique.svg

Breon, F. M., Buriez, J. C., Couvert, P., Deschamps, P. Y., Deuze, J. L., Herman, M., et al. (2002, November). Scientific results from the Polarization and Directionality of the Earth's Reflectances (POLDER). *Advances in Space Research, 30*(11), 2383-2386.

Bromba, M. U., & Ziegler, H. (1981). Application Hints for Savitzky-Golay Digital Smoothing Filters. *Analytical Chemistry, 53*, 1583-1586.

Craven, J., Kudenov, M. W., Stapelbroek, M. G., & Dereniak, E. L. (2010). Compact Infrared Hyperspectral Imaging Polarimeter. *Proceedings of SPIE, 7695*.

Dave3457. (2010, March 29). *File:Circular.Polarization.Circularly.Polarized.Light Circular.Polarizer Passing.Left.Handed.Helix.View.svg.* Retrieved May 2012, from Wikimedia Commons: http://commons.wikimedia.org/wiki/File:Circular.Polarization.Circularly.Polarized.Light_Circular.Polarizer_Passing.Left.Handed.Helix.View.svg

Deschamps, P.-Y., Nicolas, J.-M., Breon, F.-M., Moulin, C., & Bricaud, A. (1998, November). *POLDER and Ocean Color*. Retrieved May 2012, from International Ocean-Colour Coordinating Group: http://www.ioccg.org/reports/polder/polder.html

Diner, D., Hancock, B., Gutt, G., Chipman, R., & Cairns, B. (2007, December 10). Dual-photoelastic modulator-based polarimetric imaging concept for aerosol remote sensing. *Applied Optics, 46*(35), 8428-8445.

Dobos, E. (2006). Albedo. In R. Lal, *Encyclopedia of Soil Science* (2 ed., Vol. 1, pp. 64-66). CRC Press.

Escuti, M. J., Oh, C., Sanchez, C., Bastiaansen, C., & Broer, D. J. (2006). Simplified spectropolarimetry using reactive mesogen polarization gratings. *Proceedings of SPIE, 6302*.

Evans, R. (2007). Modeling of SOC-700 Hyperspectral Imagery with the CAMEO-SIM Code. *Proceedings of the 2007 Ground Systems Modeling, Validation & Testing Conference.*

Eyler, M. E. (2009). *Polarimetric Imaging for the Detection of Disturbed Surfaces.* Master's Thesis, Naval Postgraduate School.

Falk, D., Brill, D., & Stork, D. (1986). *Seeing the Light: Optics in Nature, Photography, Color, Vision, and Holography.* Wiley.

Forssell, G. (2001). Surface landmine and trip-wire detection using calibrated polarization measurements in the LWIR and SWIR. *Proceedings of SPIE, 4491,* 41-51.

Fowles, G. R. (1975). *Introduction to Modern Optics* (2nd ed.). Dover.

Gal, J., Horvath, G., & Meyer-Rochow, V. B. (2001). Measurement of the reflection-polarization pattern of the flat water surface under a clear sky at sunset. *Remote Sensing of Environment, 76,* 103-111.

Gehrels, T. (1956, March). Photometric Studies of Asteroids. V. The Light-Curve and Phase Function of 20 Massalia. *Astrophysical Journal, 123,* 331-338.

Gehrels, T., Coffeen, T., & Owings, D. (1964, December). Wavelength dependance of polarization. III. The lunar surface. *Astronomical Journal, 69,* 826-852.

Glenar, D., Hillman, J., Saif, B., & Bergstralh, J. (1994, November 1). Acousto-optic imaging spectropolarimetry for remote sensing. *Applied Optics, 33*(31), 7412-7424.

Goldstein, D. H., Chenault, D. B., & Pezzaniti, J. L. (1999). Polarimetric characterization of Spectralon. *Proceedings of SPIE, 3754*.

Goodrich, R. W., Cohen, M. H., & Putney, A. (1995, February). Spectropolarimetry. II. Circular Polarization Optics and Techniques. *Publications of the Astronomical Society of the Pacific, 107*(708), 179-183.

Gupta, N., Denes, L., Gottlieb, M., Suhre, D., Kaminsky, B., & Metes, P. (2000). Spectropolarimetric imaging using a field-portable imager. *Proceedings of SPIE, 4132,* 372-381.

Gurstelle, W. (2009). *Absinthe & Flamethrowers: Projects and Ruminations on the Art of Living Dangerously*. Chicago Review Press.

Hapke, B. (1986). Bidirectional Reflectance Spectroscopy. 4. The Extinction Coefficient and the Opposition Effect. *Icarus, 67,* 264-280.

Hapke, B. (2006, January 3). *The History of the Fairy Castles*. Retrieved May 2012, from Apollo Lunar Surface Journal: http://www.hq.nasa.gov/alsj/Fcastles.htm

Hapke, B. W., Nelson, R. M., & Smythe, W. D. (1993, April 23). The Opposition Effect of the Moon: The Contribution of Coherent Backscatter. *Science, 260*(5107), 509-511.

Hapke, B., DiMucci, D., Nelson, R., & Smythe, W. (1996). The cause of the hot spot in vegetation canopies and soils: shadow-hiding versus coherent backscatter. *Remote Sensing of the Environment, 58*, 63-68.

Hapke, B., Nelson, R., & Smythe, W. (1998). The Opposition Effect of the Moon: Coherent Backscatter and Shadow Hiding. *Icarus, 133*, 89-97.

Hapke, B., Nelson, R., Smythe, W., Gharakanian, V., Horn, L., & Lane, A. (1992). Opposition Effect and Negative Polarization: Laboratory Studies. *Lunar and Planetary Science XXIII*, 483-484.

Hecht, E. (1998). *Optics* (3rd ed.). Reading: Addison-Wesley.

Helfenstein, P., Veverka, J., & Hillier, J. (1997). The Lunar Opposition Effect: A Test of Alternative Models. *Icarus, 128*, 2-14.

Hendricks, L. (2012, April 26). SPIE Defense, Security, and Sensing 2012 Expo. (K. Foster, Interviewer)

Homma, K., Shibayama, M., Yamamoto, H., Sugahara, K., & Shingu, H. (2005). Water pollution monitoring using a hyperspectral imaging spectropolarimeter. *Proceedings of SPIE, 5655*, 419-426.

Hoya. (2012). *Skylight 1B General Filters*. Retrieved May 2012, from Hoya Filters: http://www.hoyafilter.com/products/hoya/gf-02.html

Inductiveload, X. (2007, February 12). *File:Polarisation (Circular).svg.* Retrieved May 2012, from Wikimedia Commons: http://commons.wikimedia.org/wiki/File:Polarisation_(Circular).svg

Inductiveload, X. (2007, February 12). *File:Polarisation (Elliptical).svg.* Retrieved May 2012, from Wikimedia Commons: http://commons.wikimedia.org/wiki/File:Polarisation_(Elliptical).svg

Inductiveload, X. (2007, February 12). *File:Polarisation (Linear).svg.* Retrieved May 2012, from Wikimedia Commons: http://commons.wikimedia.org/wiki/File:Polarisation_(Linear).svg

Jones, E. M. (2001, December 11). *Drilling Troubles*. Retrieved May 2012, from Apollo 15 Lunar Surface Journal: http://www.hq.nasa.gov/alsj/a15/a15.alsepdep.html#1250052

McEwen, A. S., Eliason, E. M., Bergstrom, J. W., Bridges, N. T., Hansen, C. J., Delamere, W. A., et al. (2007). Mars Reconnaissance Orbiter's High Resolution Imaging Science Experiment (HiRISE). *Journal of Geophysical Research, 112*.

McKay, D. S., Carter, J. L., Boles, W. W., Allen, C. C., & Allton, J. H. (1994). JSC-1: A New Lunar Soil Simulant. *Engineering, Construction, and Operations in Space IV*, 857-866.

Mellish, R. (2006, April 21). *File:Wire-grid-polarizer.svg.* Retrieved May 2012, from Wikimedia Commons: https://commons.wikimedia.org/wiki/File:Wire-grid-polarizer.svg

NASA. (1972, December). AS17-133-20229HR.jpg. Retrieved May 2012, from http://www.hq.nasa.gov/alsj/a17/AS17-133-20229HR.jpg

NASA. (2012). *Landsat 7 Science Data Users Handbook.*

NASA JPL. (2011, September 28). *General Overview*. Retrieved May 2012, from AVIRIS: Airborne Visible/Infrared Imaging Spectrometer: http://aviris.jpl.nasa.gov/aviris/index.html

Ottaviani, M., Merck, C., Long, S., Koskulics, J., Stamnes, K., Su, W., et al. (2008, April 1). Time-resolved polarimetry over water waves: relating glints and surface statistics. *Applied Optics, 47*(10), 1638-1648.

Pajs, X. (2007, August 5). *File:Brewsters-angle.svg.* Retrieved May 2012, 2012, from Wikimedia Commons: http://commons.wikimedia.org/wiki/File:Brewsters-angle.svg

Penubag, X. (2008, May 15). *File:Electromagnetic-Spectrum.png.* Retrieved May 2012, from Wikimedia Commons: http://commons.wikimedia.org/wiki/File:Electromagnetic-Spectrum.png

Pesses, M., Tan, J., Hash, R., & Swartz, R. (2002). Simulation of LWIR polarimetric observations of space objects. *IEEE Computer Society Proceedings of the 31st Applied Imagery Pattern Recognition Workshop*, (pp. 164-170).

Richards, J. A., & Jia, X. (2006). *Remote Sensing Digital Image Analysis: An Introduction* (4th ed.). Springer.

Schott, J. R. (2007). *Remote Sensing: The Image Chain Approach* (2nd ed.). Oxford University Press.

Schott, J. R. (2009). *Fundamentals of Polarimetric Remote Sensing.* SPIE Press.

Shaw, G. A., & Burke, H.-h. K. (2003). Spectral imaging for remote sensing. *Lincoln Laboratory Journal, 14*(1), 3-28.

Shkuratov, Y. G., Kreslavsky, M. A., Ovcharenko, A. A., Stankevich, D. G., & Zubko, E. S. (1999). Opposition effect from Clementine data and mechanisms of backscatter. *Icarus, 141*, 132-155.

Shkuratov, Y. G., Ovcharenko, A. A., Psarev, V. A., & Bondarenko, S. Y. (2008). 10. Laboratory measurements of reflected light intensity and polarization for selected particulate surfaces. In A. A. Kokhanovsky, *Light Scattering Reviews 3: Light Scattering and Reflection* (pp. 383-402). Springer Praxis Books.

Shkuratov, Y., Ovcharenko, A., Zubko, E., Miloslavskaya, O., Muinonen, K., Piironen, J., et al. (2002). The Opposition Effect and Negative Polarization of Structural Analogs for Planetary Regoliths. *Icarus, 159*, 396-416.

Surface Optics Corporation. (2001). *SOC700 & HSAnalysis2 User's Manual.* San Diego.

Taniguchi, A., Oka, K., Okabe, H., Naito, H., & Nakatsuke, N. (2006). Miniaturized Channeled Spectropolarimeter. *Conference on Lasers and Electro-Optics/Quantum Electronics and Laser Science Conference and Photonic Applications Systems Technologies.* Optical Society of America.

The Tiffen Company. (2012). *Tiffen Photar Filter Glass Catalog.*

Tiffen. (2012). *72mm Warm Polarizer Filter*. Retrieved May 2012, from Tiffen: http://www.tiffen.com/displayproduct.html?tablename=filters&itemnum=72WPOL

Tishkovets, V. (1997). Negative polarization of light scattered by closely packed disperse media. *Lunar and Planetary Science XXVIII.*

Tonizzo, A., Zhou, J., Gilerson, A., Twardowski, M. S., Gray, D. J., Arnone, R. A., et al. (2009, March 30). Polarized light in coastal waters: hyperspectral and multiangular analysis. *Optics Express, 17*(7), 5666-5683.

Tyo, J. S., Goldstein, D. L., Chenault, D. B., & Shaw, J. A. (2006, August 1). Review of passive imaging polarimetry for remote sensing applications. *Applied Optics, 45*(22), 5453-5469.

Webb, R. H. (1997). *Elementary Wave Optics.* Dover.

Woessner, P., & Hapke, B. (1987). Polarization of Light Scattered by Clover. *Remote Sensing of Environment*, *21*, 243-261.

Wolff, M. (1975, June). Polarization of light reflected from rough planetary surface. *Applied Optics, 14*(6), 1395-1405.

Zubko, E., Videen, G., Shkuratov, Y., Muinonen, K., & Yamamoto, T. (2011). The Umov effect for single irregularly shaped particles with sizes comparable with wavelength. *Icarus, 212*(1), 403-415.

ABOUT THE AUTHOR

Kyle A. Foster graduated from Paul V. Moore High School in Central Square, New York in 2003. He completed his Bachelor of Science degree in Imaging Science from the Rochester Institute of Technology in Rochester, New York in 2008. Since 2007, he has worked as an image scientist in Northern Virginia; first with ITT Geospatial Systems (formerly ITT Space Systems Division), and since 2011 for The Boeing Company. He received his Master of Science in Earth Systems Science from George Mason University in 2012, earning the Department of Geography and GeoInformation Sciences Outstanding MS Graduate Student Award. At time of writing, Kyle resides in Northern Virginia with his wife Courtney, his daughter Claire, and their two cats, Indy and Sallah.